โครงการ

การเรียนการสอนเพื่อเสริมประสบการณ์

ชื่อโครงการ	การสังเคราะห์นิกเกิลออกไซด์-ทองบนวัสดุคอมพอสิตของอนุภาคแม่เหล็กระดับนาโน-ไฮดรอกซีอะพาไทต์เพื่อเป็นตัวเร่งปฏิกิริยาเชิงแสงสำหรับการสลายสีย้อม
	Synthesis of Nickel Oxide-Gold Supported on Magnetic Nanoparticle-Hydroxyapatite Composites to Use as a Photocatalyst for Dye Degradation
ชื่อนิสิต	นางสาวอาภากร ผาสุข
ภาควิชา	เคมี
ปีการศึกษา	2559

คณะวิทยาศาสตร์ จุฬาลงกรณ์มหาวิทยาลัย

Synthesis of Nickel Oxide-Gold Supported on Magnetic Nanoparticle-Hydroxyapatite Composites to Use as a Photocatalyst for Dye Degradation

การสังเคราะห์นิกเกิลออกไซด์-ทองบนวัสดุคอมพอสิตของอนุภาคแม่เหล็กระดับนาโน-ไฮดรอกซีอะพาไทต์เพื่อเป็นตัวเร่งปฏิกิริยาเชิงแสงสำหรับการสลายสีย้อม

by

Miss Apakorn Phasuk

This report is a partial fulfillment of the requirements for the degree of Bachelor of Science Program in Chemistry Chulalongkorn University Academic year 2016

Project Title: Synthesis of Nickel Oxide-Gold Supported on Magnetic Nanoparticle-Hydroxyapatite Composites to Use as a Photocatalyst for Dye Degradation
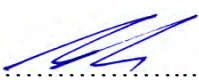
By: Miss Apakorn Phasuk

Accepted by Department of Chemistry, Faculty of Science, Chulalongkorn University in Partial Fulfillment of the Requirements for the Degree of Bachelor of Science Program in Chemistry

…………………………………. Head of Department of Chemistry

(Assoc. Prof. Vudhichai Parasuk, Ph.D.)

…………/………….………

PROJECT COMMITTEE

……………………………..………. Chair Committee

(Assoc. Prof. Sumrit Wacharasindhu, Ph.D.)

…………………………………….... Project Advisor

(Wipark Anutrasakda, Ph.D.)

………………………………….…... Committee

(Numpon Insin, Ph.D.)

Quality of the following work is rated: ☑ Excellent   ☐ Good   ☐ Average

ชื่อโครงการ   การสังเคราะห์นิกเกิลออกไซด์-ทองบนวัสดุคอมพอสิตของอนุภาคแม่เหล็กระดับ
                       นาโน-ไฮดรอกซีอะพาไทต์เพื่อเป็นตัวเร่งปฏิกิริยาเชิงแสงสำหรับการสลายสีย้อม

ชื่อนิสิตในโครงการ   นางสาวอาภากร ผาสุข   เลขประจำตัว 5633173323
ชื่ออาจารย์ที่ปรึกษา   อาจารย์ ดร.วิภาค อนุตรศักดา
ภาควิชาเคมี คณะวิทยาศาสตร์ จุฬาลงกรณ์มหาวิทยาลัย ปีการศึกษา 2559

บทคัดย่อ

งานวิจัยนี้มุ่งเน้นการสังเคราะห์สารประกอบชนิดใหม่ของนิกเกิลออกไซด์-ทองบนวัสดุคอมพอสิตของ
อนุภาคแม่เหล็กระดับนาโน-ไฮดรอกซีอะพาไทต์ด้วยวิธีตกตะกอนร่วมและการเคลือบฝัง เพื่อใช้ศึกษา
ความสามารถในการเป็นตัวเร่งปฏิกิริยาเชิงแสงภายใต้แสงที่ตามองเห็นได้ โดยอนุภาคทองขนาดนาโนถูก
นำมาใช้ในสารประกอบเพื่อเพิ่มประสิทธิภาพในการเร่งปฏิกิริยาเชิงแสงด้วยสมบัติโลคอลไลซ์พลาสมอนเร
โซแนนซ์ที่พื้นผิว ในขณะที่อนุภาคแม่เหล็กระดับนาโนถูกนำมาใช้เพื่อความสะดวกในการแยกสารประกอบ
ออกจากปฏิกิริยาด้วยสนามแม่เหล็กภายนอก ผลจากการพิสูจน์เอกลักษณ์ของสารประกอบพบว่า สามารถ
ยืนยันผลึกของอนุภาคแม่เหล็ก ไฮดรอกซีอะพาไทต์ และนิกเกิลออกไซด์ในสารประกอบได้ด้วยเทคนิค
XRD และสามารถยืนยันการมีอยู่ของอนุภาคทองระดับนาโนบนคอมพอสิตได้ด้วยเทคนิค TEM โดย
อนุภาคทองมีขนาดเฉลี่ยเท่ากับ 3.3 นาโนเมตร ในขณะที่ปริมาณทองและนิกเกิลในสารประกอบสามารถ
หาค่าได้จากเทคนิค ICP-OES

ผลการทดสอบสมบัติการเป็นตัวเร่งปฏิกิริยาเชิงแสงของสารประกอบที่สังเคราะห์ได้โดยใช้เมทิลี
นบลูเป็นสีย้อมตัวอย่างพบว่า สีย้อมถูกกำจัดประมาณร้อยละ 56 ภายใต้กระบวนการเร่งปฏิกิริยาเชิงแสง
ในขณะที่การทดสอบปฏิกิริยาเชิงแสงด้วยสภาวะเดียวกันแต่ไม่เติมสารประกอบที่สังเคราะห์ได้พบว่า ร้อย
ละของสีย้อมที่ถูกกำจัดมีค่าใกล้เคียงกัน ซึ่งจากการค้นพบนี้ชี้ให้เห็นว่าการเร่งปฏิกิริยาของสารประกอบที่
สังเคราะห์ได้ภายใต้แสงเหนือม่วงหรือแสงที่ตามองเห็นไม่มีผลต่อการสลายตัวของเมทิลีนบลู จากการ
ทดลองเพิ่มเติมพบว่า การสลายตัวของเมทิลีนบลูไม่ถูกเหนี่ยวนำด้วยความร้อน แต่มีแนวโน้มที่เมทิลีนบลู
สามารถสลายตัวเองได้หากใช้เวลาในการทำปฏิกิริยานานเพียงพอภายใต้แสงที่ตามองเห็น (มากกว่า 2
ชั่วโมง) โดยสาเหตุที่สารประกอบที่สังเคราะห์ได้ไม่สามารถทำหน้าที่เป็นตัวเร่งปฏิกิริยาเชิงแสงอาจเป็นผล
มาจากการไม่ทับซ้อนกันระหว่างแถบพลังงานของนิกเกิลออกไซด์และไฮดรอกซีอะพาไทต์

คำสำคัญ: ตัวเร่งปฏิกิริยาเชิงแสง, นิกเกิลออกไซด์, ไฮดรอกซีอะพาไทต์, ทอง, อนุภาคแม่เหล็กระดับนาโน

Project Title Synthesis of Nickel Oxide-Gold Supported on Magnetic Nanoparticle-Hydroxyapatite Composites to Use as a Photocatalyst for Dye Degradation

Student Name Miss Apakorn Phasuk Student ID 5633173323

Advisor Name Wipark Anutrasakda, Ph.D.

Department of Chemistry, Faculty of Science, Chulalongkorn University, Academic Year 2016

Abstract

A novel composite of nickel oxide-gold supported on magnetic hydroxyapatite nanocomposite (Au-NiO-HAp@γ-Fe$_2$O$_3$) was successfully synthesized *via* a combination of co-precipitation and impregnation methods. The application as a photocatalyst for organic dye degradation under visible light was investigated. Gold nanoparticles (AuNPs) were incorporated into the composite in order to improve the photocatalytic activity via localized surface plasmon resonance. Magnetic nanoparticles (γ-Fe$_2$O$_3$) were also incorporated in order to allow easy and rapid magnetic separation of the photocatalyst through the application of an external magnetic field. Crystalline phases of γ-Fe$_2$O$_3$, HAp, and NiO were confirmed by XRD. The presence of AuNPs with the size of 3.3 nm was confirmed by TEM. The amount of Au and NiO in the composites was determined by ICP-OES.

The photocatalytic performance of the synthesized magnetic composite was investigated using methylene blue (MB) as a model dye. Approximately 56% of MB was removed during the photocatalytic process. Nevertheless, in an analogous experiment performed without Au-NiO-HAp@ γ-Fe$_2$O$_3$, similar removal percentage of MB was obtained. This finding indicated that the intended catalytic process, either under UV light or visible light, did not significantly affect the degradation of MB. Further experiments revealed that the removal of MB was also not induced by heat derived from the system. Instead, the degradation of MB likely resulted from its self-photolysis that occurred during a sufficiently long reaction time (> 2 h). The failure of Au-NiO-HAp@ γ-Fe$_2$O$_3$ to catalyze the degradation of MB may in part be attributable to the effect of non-overlapping frontier electronic bands of NiO and HAp.

Keyword: Photocatalyst, nickel oxide, hydroxyapatite, gold, magnetic nanoparticles
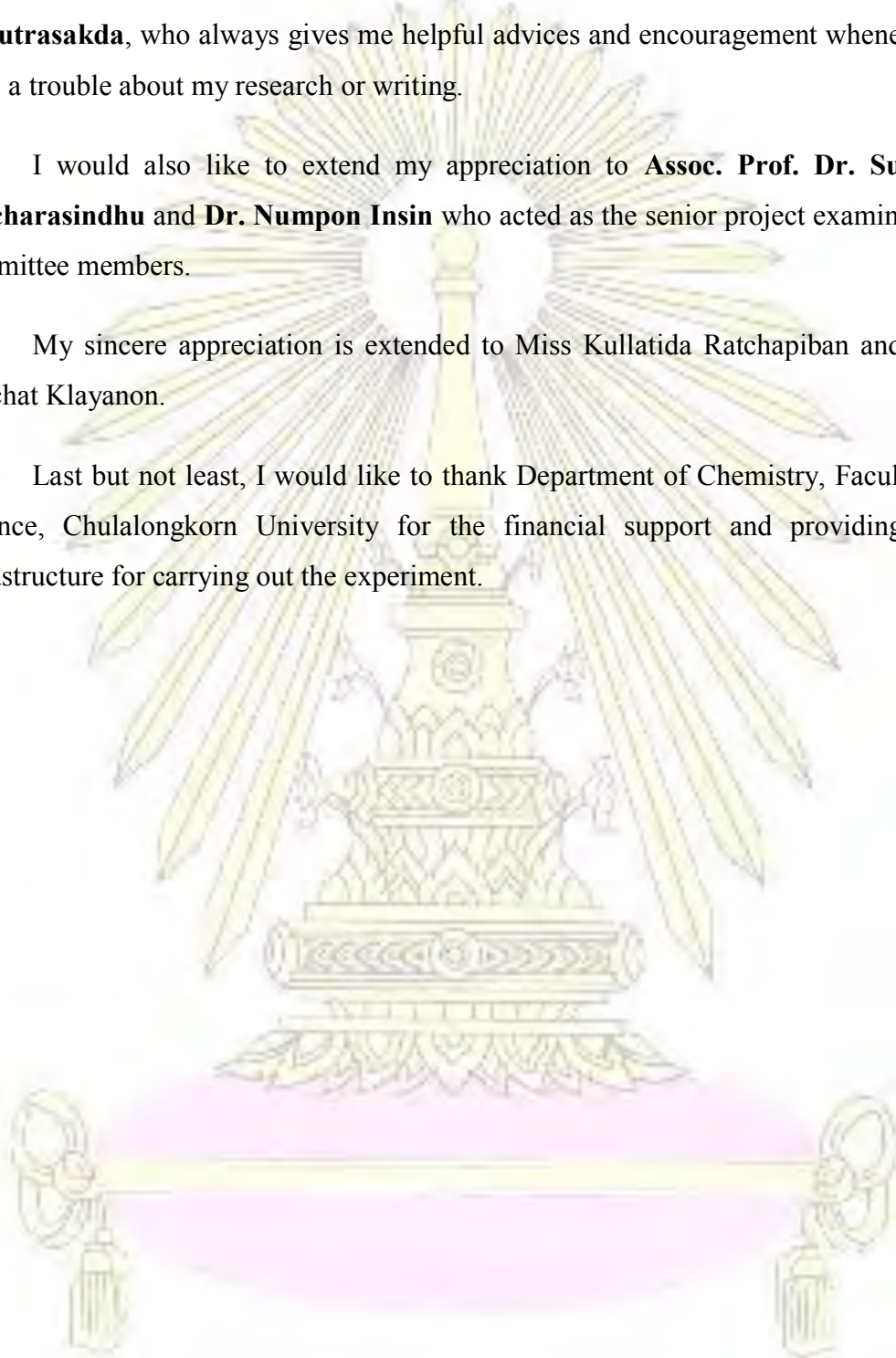
Acknowledgment

Contents

Index of Tables

Index of Figures

List of Abbreviations

MB	methylene blue
MO	methyl orange
mg	milligram
mL	milliliter
μm	micrometer
ppm	part per million
AOP	advanced oxidation process
LSPR	localized surface plasmon resonance
AuNP	gold nanoparticle
HAp	hydroxyapatite

Chapter 1

Introduction

1.1 Background and motivation

Nowadays, many industries such as paper, plastic, and textile, use organic substances as an additive to modify and decorate products, or as one part of production process. In general, one of the most popular organic substances used widely in industrial is dyes which make materials colorful. However, dyes have been lost in many processes into wastewater, accounting for 15 percent of total dyes. Dyes are also known as an environmental pollutant and harmful to aquatic creatures. Therefore, wastewater should be treated before releasing.[1] There are several methods to treat wastewater, including filtration, precipitation, and adsorption. Unfortunately, these methods are high-cost and generate toxic products. Therefore, a cheaper and higher efficient method is required. One of high-efficient methods to eliminate these pollutants is 'Advanced Oxidation Process or AOP' which uses reactive oxygen species, such as hydroxyl radical, peroxide, and superoxide, as a redox-active agent in the reaction.[2] AOP can be divided into two types: (1) the homogeneous system using hydrogen peroxide, ozone or ultraviolet (UV) light (2) the heterogeneous system using metal oxide as a semiconductive catalyst. We are particularly interested in the latter because the catalyst can be separated easily from reactants after the reaction completed.

The most frequently used semiconductive photocatalyst is titanium dioxide (TiO_2), which is non-toxic and has high catalytic activity; but it has two major drawbacks. Firstly, titanium dioxide has high rate of electron-hole recombination, lowering its catalytic activity. Secondly, pristine TiO_2 can be only used with UV light because of its wide band gap (3.2 eV).[3] Although researchers try to solve these problems by modifying TiO_2-based catalysts in order to use them in visible light region, the modified processes are quite complicated and required high-priced reagents.[4]

Compared to TiO_2, nickel oxide (NiO) possesses a semiconductive ability with relatively narrower band gap, which increases its photocatalytic potential in visible light region.[3] Furthermore, to achieve highest catalytic performance, we are interested in making a composite of NiO with gold nanoparticles (AuNPs), which can also absorb

visible light and generate electron-hole pair *via* 'Localized Surface Plasmon Resonance or LSPR'. Electrons generated by AuNPs can relocate to nearby semiconductive particles, on which redox reactions subsequently occur. To the best of our knowledge, this work is among the first to combine AuNPs with NiO to use in photocatalytic reaction. Previously, there are many researches using AuNPs to enhance photocatalytic activity of TiO_2 toward degradation of small organic molecules[5] and dyes[6]. Thus, we hypothesize that AuNPs could improve the photocatalytic ability when combined with NiO in the same composite.

Nevertheless, the NiO-AuNPs composite may have a limitation due to its tendency to aggregate; hence, lowering the surface area and catalytic performance. To solve this problem, hydroxyapatite (HAp), is used as a supporting material to prevent aggregation of the NiO-AuNPs composite and to increase surface area of the catalyst. Calcium ions in hydroxyapatite structure can be substituted by other cations with similar ionic radius, enabling the impregnation of metal and metal oxide onto HAp possible. Moreover, HAp is a very stable and inert adsorbent which is expected to promote the catalytic activity of the supported catalysts.[7]

In addition, some researchers reported that supports and catalysts might have band gap overlapping, causing the change in band gap of the composite. In case of hydroxyapatite, its band gap is 3.6 eV and is expected to cause the band gap of the composites to be wider.[8] For example, absorption spectrum of titania composite with hydroxyapatite will undergo hypsochromic shift because of band gap overlapping. As shown in Figure 1.1, the energy gap of TiO_2 partially overlaps with that of NiO. Therefore, we expect that energy gap of nickel oxide will undergo hypsochromic shift in the same manner. When we focus on absorption spectrum of nickel oxide (Figure 1.2), it has a broad peak between 650 and 800 nm which is in near-infrared region. If this peak undergoes hypsochromic shift, the broad peak will shift to visible light region, so nickel oxide can take more advantage of visible light to initiate AOP. For our country, Thailand get much sunlight, which has the highest radiation intensity at around 500 nm, so catalysts that can be used in visible light are more beneficial than catalysts that require UV light to operate.
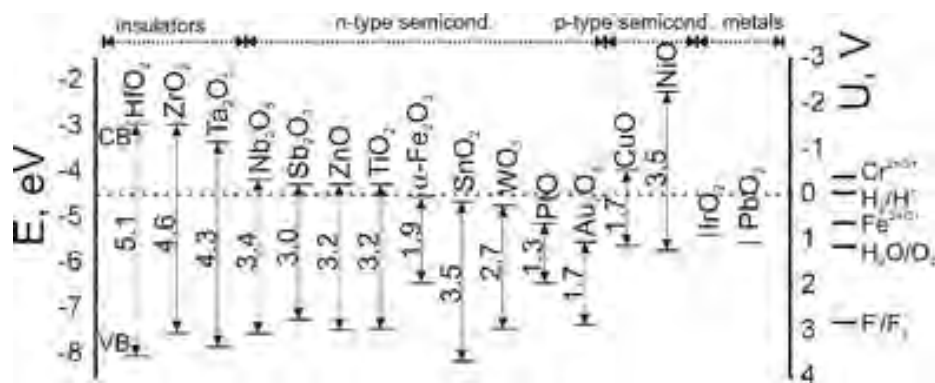
Figure 1.1 Energy levels of metal oxides.[9]
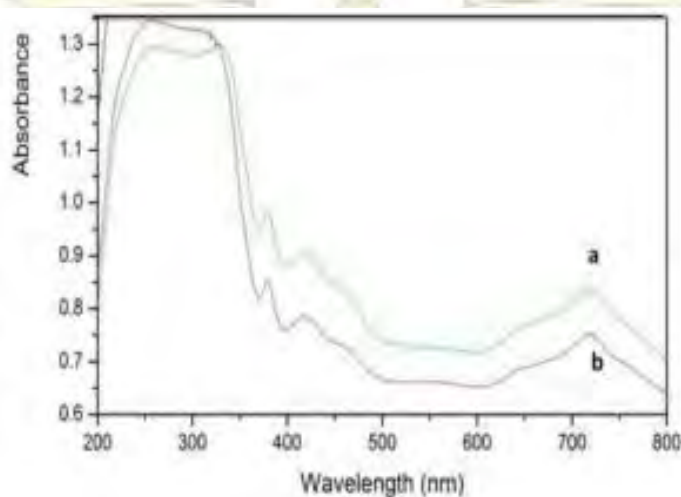
Figure 1.2 Absorption spectrum of nickel oxide a) NiO calcined at 450°C b) NiO calcined at 600°C.[3]

Even if our proposed catalyst is a heterogeneous catalyst, which is easy to be separated, its small size makes it more difficult to be separated from the reaction mixture by centrifugation. In this work, we plan to composite magnetic nanoparticle which has superparamagnetic property with our proposed catalyst to make it easier to be removed after the reaction completed. One of interesting superparamagnetic materials is γ-Fe_2O_3 particle because it exhibits paramagnetic character, so it can be well-dispersed in the solution during the reaction period. Also, it contains magnetic property when it is induced by the external magnetic field, so it can be conveniently separated from the mixture by a magnet. However, when the time passes, superparamagnetic particles can aggregate with each other and loses their magnetic

property. Therefore, to solve this problem, a supporting material is required to prevent the particle aggregation.[10]

In this research, we focus on synthesis of novel nickel oxide-gold supported on magnetic nanoparticle-hydroxyapatite composites to use as a photocatalyst for dye degradation under visible light condition.

1.2 Objectives

1. Synthesizing novel nickel oxide-gold supported on magnetic nanoparticle-hydroxyapatite composites.

2. Testing photocatalytic activity of the synthesized nickel oxide-gold supported on magnetic nanoparticle-hydroxyapatite composites for dye degradation.

1.3 Expected outcomes

1. Obtaining novel nickel oxide-gold supported on magnetic nanoparticle hydroxyapatite composites.

2. Obtaining optimum conditions of dye degradation using the synthesized nickel oxide-gold supported on magnetic nanoparticle-hydroxyapatite composites as a photocatalyst.

1.4 Theory and related literatures

1.4.1 Semiconductor and semiconductor photocatalysis

In chemistry, a semiconductor is defined as a material whose energy gap for electronic transition is in between that of insulator and conductor. Unlike that of metal which is a conductor, the valence band of semiconductor does not overlap with the conduction band. Thus, semiconductor cannot conduct electricity because electrons in the valence band cannot move around. However, when semiconductor gets some energy from external sources (e.g., thermal energy and electromagnetic radiation), some of its electrons from the valence band will absorb that energy and jump to the vacant conduction band and thus can move freely. There are several renowned semiconducting materials having been used by researchers such as TiO_2, ZnO, and CdS. Each material has a characteristic energy gap depending on its shape, size, dopants, etc. Therefore, materials having a specific energy gap can be designed by varying these properties.

Because of this versatility, semiconductors have been widely used in electronic and chemical applications.[11]

When electronic transition occurs in semiconductor, it not only produces free electrons in the conduction band but also generates positive holes in the valence band. In the presence of water, a free electron can reduce a water molecule, generating hydrogen peroxide species; and a positive hole can act as an oxidizing agent to convert a water molecule to hydroxyl radical species. These two species possess high reactivity to undergo oxidation processes with organic substances, such as organic dye molecules, to mineralize organic compounds into inorganic substances (e.g. nitrates, phosphates, carbon dioxide, water, etc.) (Figure 1.3) which have less toxicity and can be used and recycled by plants and scavengers. The term 'Semiconductor Photocatalysis' is used for the process that uses a semiconductor as a catalyst and light as an energy source (Figure 1.4). The oxidation processes evolving these reactive oxygen species are also known as 'Advanced Oxidation Processes or AOPs'.[12]
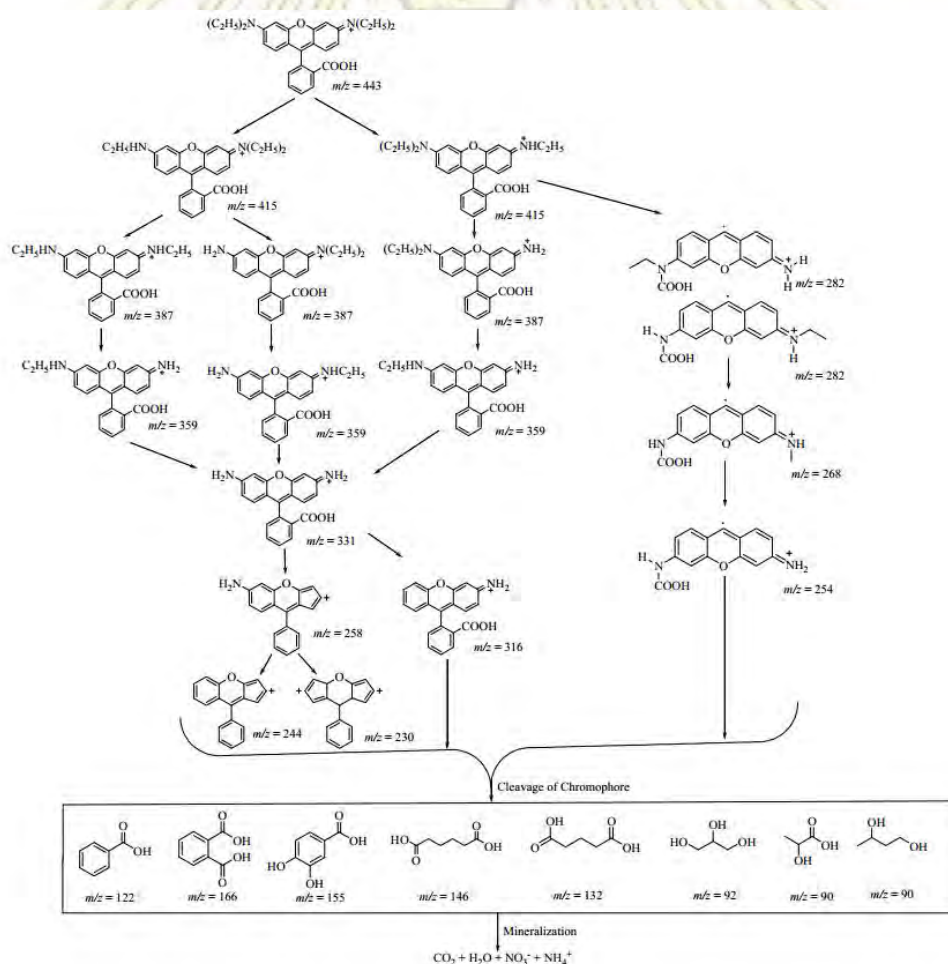
Figure 1.3 Mineralization mechanism caused by radical oxidation process.[13]
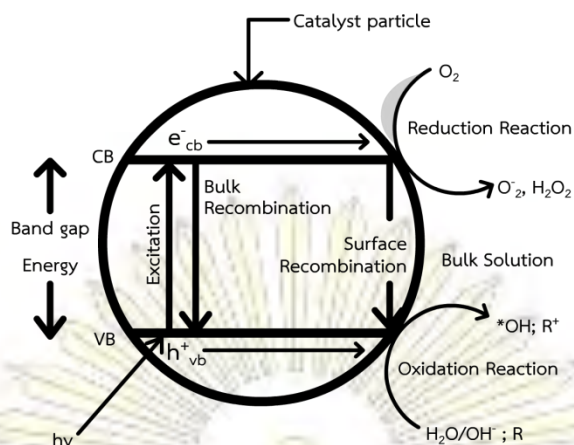
Figure 1.4 Photocatalytic mechanism of a semiconductor.

1.4.2 Localized surface plasmon resonance (LSPR)

Plasmon resonance is a phenomenon that free charge of conducting materials oscillates when the conducting materials absorb electromagnetic wave at the same frequency as material natural frequency. The light with a longer wavelength will be reflected because of electron screening, while the light with a shorter wavelength will pass through the material because of slow screening time of electron. Plasmon effect is categorized into two types: a) surface plasmon resonance which can be further classified into localized surface plasmon resonance and general surface plasmon resonance, and b) volume plasmon resonance. In this research, we focus only on localized surface plasmon resonance.

Localized surface plasmon resonance is a fascinating optical property of metal nanoparticles, occurring when electrons confined around the nanoparticle absorb energy from light at the wavelength equals to its natural oscillation frequency (Figure 1.5). Consequently, the electrons oscillate and thus induce an intent electric field around the nanoparticle which can enhance the photocatalytic process via many methods such as charge transfer, local electric field enhancement, light absorption, electromagnetic simulation and doping. Furthermore, the frequency of this resonance depends on many factors such as size, shape, and type of materials. The smaller size leads to the longer frequency. For example, when gold nanoparticle is minimized in size, its plasmon frequency is shifted from visible to infrared region (Figure 1.6).[14–16]
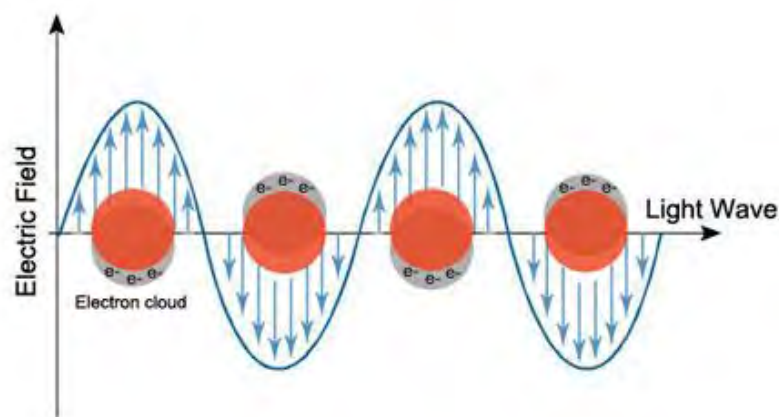
Figure 1.5 Basics of localized surface plasmon resonance (LSPR) of gold nanoparticles due to collective oscillation of surface electrons with incident light at a specific wavelength.[14]
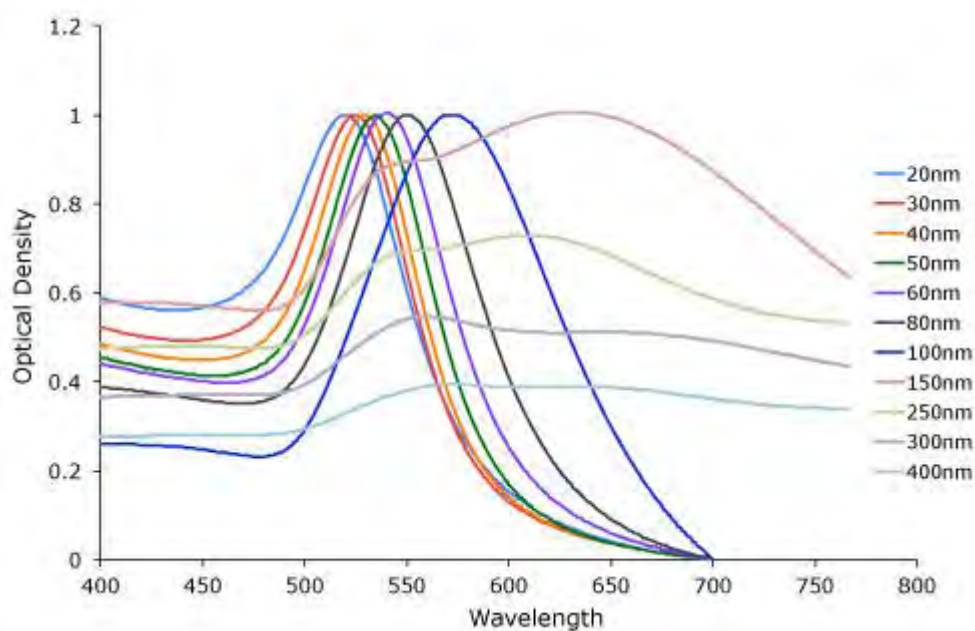
Figure 1.6 Gold nanoparticle size dependent surface plasmon resonance. Note the red-shift of the absorption maximum as the gold nanoparticle size increases.[14]

1.4.3 Optical spectroscopy

The principle of optical properties is based on Bohr-Einstein equation in which energy is proportional to frequency (Equation 1.1). The discrete energy state of atom and molecule is linked with appropriate specific frequency. In addition, optical properties include reflection, refraction, transmission, absorption, and emission. In this

work, we focus on absorption and emission properties to characterize synthesized materials and to investigate dye degradation.

$$\Delta E = E_2 - E_1 = h\nu \qquad \text{(Equation 1.1)}$$

Where

ΔE is the energy between ground state and excited state of atom and molecule. (J)

E_1 and E_2 are energy levels of initial state and final state of atom and molecule. (J)

h is Planck's constant. $(6.626 \times 10^{-34} \text{ J s})$

ν is frequency of electromagnetic radiation. (s^{-1})

1.4.3.1 Absorption spectroscopy

Absorption occurs when an electron in HOMO absorbs light energy equals to the energy gap of the molecule and is subsequently excited to LUMO. Since each compound has a specific energy gap, researchers can use absorption spectrometry to qualitatively identify the molecule. Moreover, absorption ability (i.e. absorbance) of diluted substances in gaseous and aqueous states follows the Beer-Lambert law (Equation 1.2), which states that there is a linear correlation between the concentration of the molecule and the absorbance. Therefore, we can determine the concentration of the substrate using a calibration curve.

$$\log\frac{I_0}{I} = A = \varepsilon \cdot c \cdot b, \qquad \text{(Equation 1.2)}$$

where

A is the absorbance.

ε is the molar extinction coefficient. $(M^{-1} \text{ cm}^{-1})$

b is the path length (the length of the sample through which the light passes). (cm)

c is the concentration of the sample. (M)

I_0 is the intensity of the monochromatic light entering the sample; and I is the intensity of the light emerging from the sample.

In case of the absorption in ultraviolet (UV) and visible light (Vis) region, the electromagnetic radiation in this range is consistent with the energy difference of

electronic state of molecule. Therefore, the frequency regions are widely used by scientists in many methods of measurement. As mentioned above, molecule will absorb light at a specific wavelength. The specific wavelength and molar extinction coefficient depend on molecular structure, geometry, and symmetry of the molecule. Moreover, absorption spectrum can give information about normal vibrations coupled to electronic excitation and about the change of molecular structure, geometry, and its symmetry. Therefore, we can qualitatively investigate substances using this technique.[17]

The purpose of a spectrophotometer is to provide a beam monochromatic light to illuminate the sample and then measure the ratio of I and I_0. To do so, a typical spectrophotometer will consist of the components as illustrated in Figure 1.7.
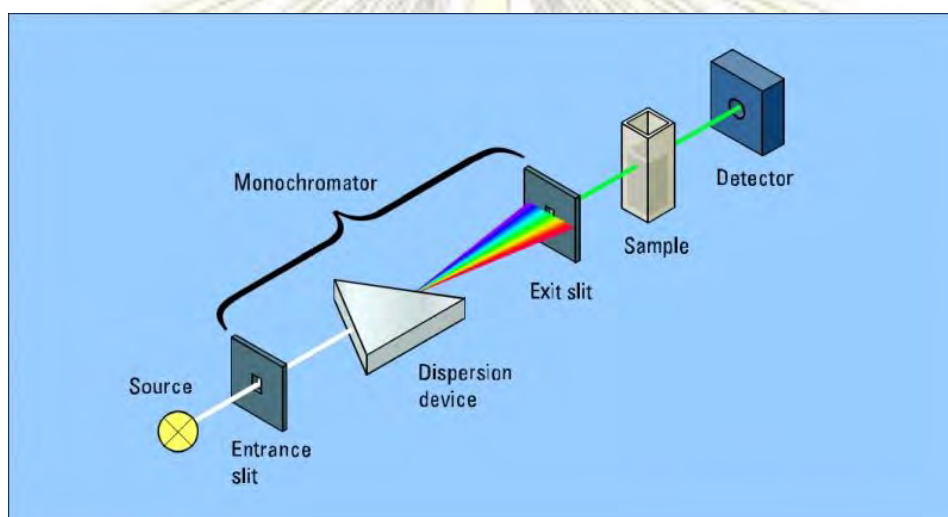
Figure 1.7 Schematic diagram of a spectrophotometer.[18]

As the light sources provide broad spectrum of light, a monochromator (such as filter, prism and slits, or grating) is required to select a specific wavelength of light. The monochromatic light is partially absorbed as it passes through the sample and eventually reaches the detector, which converts optical signal (photons) into electrical current (electrons). The generated electrons are subsequently amplified by photomultiplier tube; and the readout is finally shown on the screen.

1.4.3.2 Atomic emission spectroscopy (AES)

Emission is a phenomenon that an excited electron in an excited state of molecule or atom undergoes relaxation process by emitting the energy such as electromagnetic wave and heat to reduce its energy and goes down to ground state of

the molecule or atom. Since each atom or molecule has its own discrete energy level, the emission spectrum can be used as a fingerprint to identify the presence of elements or molecules. The molecular emission spectroscopy is known as 'fluorescence spectroscopy' which uses the electromagnetic radiation to excite an electron. On the other hand, atomic emission spectroscopy uses thermal radiation (heat) to disintegrate molecule and excite an electron. There are two major sources of heat used in atomic emission spectrometer: flame and plasma. Although flame is cheaper and easier to be made, it has major problems regarding the incomplete disintegration of compounds and oxide formation which leads to inaccurate results.

Plasma is an ionized gas that is macroscopically neutral. An external electric field is necessary to ionize the gas and sustain the plasma, which will eventually give some of its energy to the sample to atomize, ionize, and excite it. The gas that is used to generate plasma is argon, which is chemically inert. The most popular method nowadays to generate the electric field is to apply radio frequency through a coil surrounding the gas, which produces the 'inductively coupled plasma (ICP)'. Ionization of argon gas is initiated by a spark from tesla coil. The radio frequency accelerates electrons in the surrounded coil, generating fluctuate magnetic field which subsequently accelerates the electrons in argon gas. High speed electrons then collide with argon atoms to initiate further ionization which causes a rapid rise in temperature (i.e. ohmic heat). The temperature of the plasma torch can be as high as 10,000 K which can atomize and excite most of elements in the periodic table.[19]
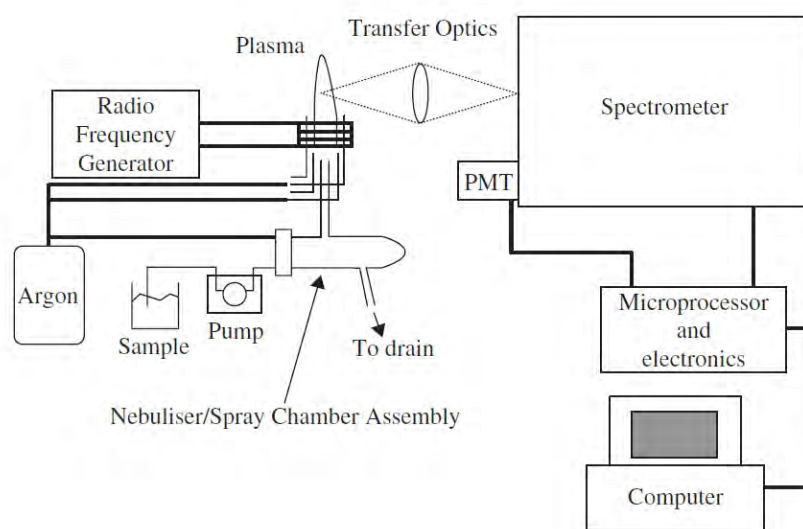
Figure 1.8 A schematic diagram of a generalized ICP-AES instrument.[19]

Apart from the plasma torch and radio-frequency generator, ICP-AES instrument is composed of a sample introduction system, a spectrometer, and a detector (Figure 1.8). The conventional sample introduction system is an assembly of nebulizer and spray chamber. Nebulizer turns the sample solution into aerosols, which are sprayed into the spray chamber; and some of them will reach the plasma torch. Typical spectrometer used in ICP-AES instrument is polychromator which can analyze several analytes simultaneously. Instead of normal grating used in monochromator, polychromator contains special grating called 'echelle grating' which reflects, separates, and converts light at all wavelengths into 2D arrays called 'echellogram' (Figure 1.9).
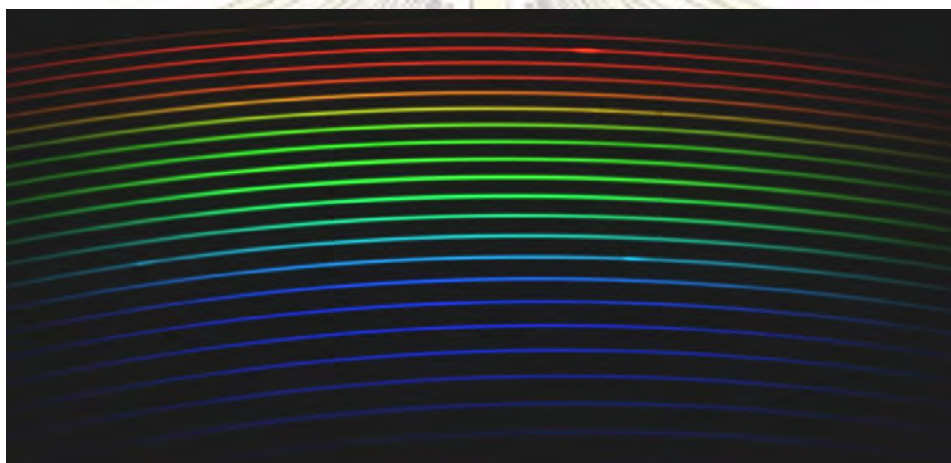
Figure 1.9 An echellogram.[20]

After that, light at each wavelength is converted into signal. In modern ICP-AES instrument, this can be done using solid-state detectors, such as CCDs (charge coupled devices) and CIDs (charge injection devices). Both are the arrays of metal oxide semiconductors which can collect photo-generated charges (CCDs collect electrons while CIDs collect holes). The light with particular wavelength coming from echelle grating will hit the specific CCD unit, so ICP-AES can measure signals from several wavelengths, thus several elements at once.

1.4.3.3 X-ray powder diffraction

X-ray powder diffraction is a non-destructive technique used to identify phase of crystalline materials. It provides information on structures, phases, crystal orientations, and other structural parameters (grain size, strain, and crystal defects). X-

ray diffraction peaks are produced by constructive interference of a monochromatic beam of X-rays scattered at specific angles from each set of lattice planes in a sample. The peak intensities are determined by the distribution of atoms within the lattice. Therefore, the X-ray diffraction pattern is the fingerprint of periodic atomic arrangements in a given material.

The principle of this technique is materials with different unit cell parameters will give different signals because they have different planes in crystal structures following Bragg's equation (Equation 1.3):

$$2d \sin \theta = n\lambda \qquad \text{(Equation 1.3)}$$

where

n is an integer.

λ is the wavelength of the X-rays. (Å)

d is the interplanar spacing generating the diffraction. (Å)

θ is the diffraction angle. (degree)

Conversion of the diffraction peaks to d-spacing allows identification of the compound because each compound has a set of unique d-spacings. Typically, this is achieved by comparison of d-spacings with standard reference patterns.

The XRD instrument can be divided into three major components: an X-ray source, a sample holder, and a detector (Figure 1.10). The most popular X-ray source is a metallic copper cathode ray tube which emits the X-ray at a specific wavelength of 1.5418 Å. These X-rays are collimated (i.e. without divergence) and directed onto the sample. The sample holder and/or the detector can be rotated so constructive interferences at every angle are possible. As the sample and/or the detector are rotated, the intensity of the reflected X-rays is recorded. The recorded signal is then converted to a count rate, which is subsequently shown on the monitor.[21]
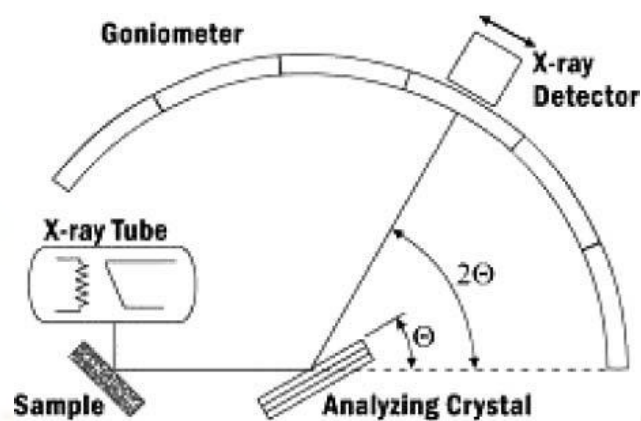
Figure 1.10 The schematic diagram of XRD instrument.[21]

1.4.4 Transmission electron microscope (TEM)

To observe things, human uses eyes which are sensitive to electromagnetic radiation in the visible region (400-700 nm) of the spectrum; and this works well in most cases. However, the spatial resolution of images observed by human eyes is only about 3 μm. Thus, a microscope is needed for object smaller than that. Typical optical microscope can 'see' an object in the range of several hundreds of nanometers because the spatial resolution of the microscope cannot be smaller than the wavelength of visible light. Since the wavelength of electrons is in picometer region (according to de Broglie's equation), an electron microscope is more powerful, with a magnification ratio from thousands to millions. Therefore, the electron microscope is an important tool to characterize the morphology of nanosized objects.

The instrument can be divided into three sections: an illumination system, a specimen stage, and an imaging system (Figure 1.11). The illumination system consists of the electron gun, which generates a beam of electrons that have sufficient energy to pass through thin TEM specimens, and magnetic condenser lenses that focus the electrons onto the specimens. In general, electrons are emitted from hot tungsten filament (or some materials with low work function, such as LaB_6) in vacuum, then pass through a small hole with adjustable negative potential which allows users to control the emission current of the electron gun. After that, electrons are accelerated to their final kinetic energy by an electric field generated by positive anode. Subsequently, electrons move through a series of two or more condenser lenses. The first condenser lens can demagnify and brighten the image in case of viewing larger areas of specimens, which requires less magnification power. The second condenser lens contains the

aperture (like a tiny hole just under the specimen holder of optical microscope) which controls the contrast of the image by adjusting the diameter of illumination.
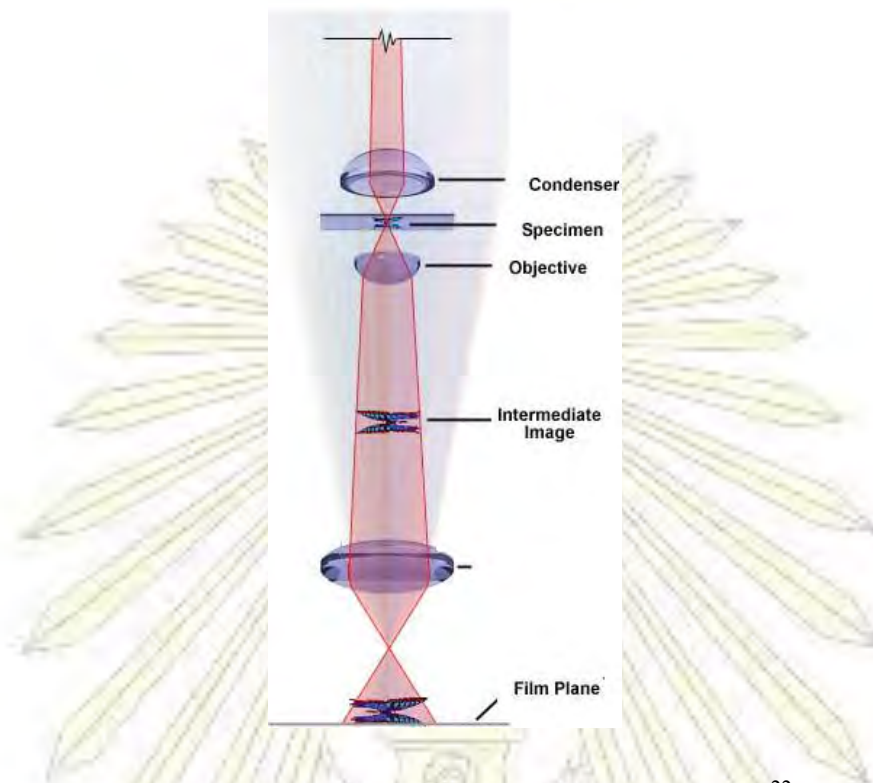
Figure 1.11 Schematic diagram of TEM instrument.[22]

The specimen stage is designed to prevent any kind of unintended specimen movement (e.g. drift and vibration) which would be magnified and degrade the final image, yet allows users to move the specimen in order to view all possible regions. Another important feature of the stage is it must allow the specimen to be inserted into the vacuum of the TEM column without letting air come in. This is achieved by using an 'airlock', which is a chamber into which the specimen is inserted and can be evacuated before sending the specimen into the TEM column. Specimen cooling can also be done here by introducing a metal rod whose another end is immersed in liquid nitrogen.

The imaging system comprises an objective lens, a projector lens, and a screen (or camera). The objective lens produces a magnified real image of the specimen. The objective lens is probably the most important part of TEM because its design and quality of this lens largely affect the resolution of the image. The projector lens is used to produce an image on the screen with fixed final image diameter. In some instruments, there are intermediate lenses in between the objective and the projector lens. There are

two purposes of the intermediate lens: further adjusts the image magnification, and allows an electron diffraction pattern to be projected onto the screen.[23]

1.4.5 Review of related literature and studies

The efficient semiconductors which are widely used in photocatalyst field for dye degradation are titania (TiO_2) and zine oxide (ZnO). In 2012, Badawy *et al.*[24] compared photocatalytic activity of azo dye degradation of TiO_2 and ZnO with reactive red 15 which is one of azo dyes. They found that the concentration of reactive red 15 decreased 87.8 and 90.5 percent after 90 minutes of UV light irradiation when TiO_2 and ZnO was used as a catalyst, respectively. This work illustrates that TiO_2 and ZnO have exceptional photocatalytic activity under UV light. In 2013, Shin *et al.*[25] synthesized flower-like ZnO nanomaterials and used them to catalyze the photodegradation of rhodamine 6G under UV light. They found that rhodamine 6G was completely mineralized into less harmful chemicals within 60 minutes.

There are also some literatures demonstrating the photocatalytic ability of TiO_2 on supporting materials. For example, in 2013, Wei *et al.*[26] prepared TiO_2 supported on hydroxyapatite material and used it as a catalyst to degrade pentachlorophenol. The results showed that supported TiO_2 and non-supported TiO_2 microsphere had similar photocatalytic ability. Nonetheless, the supported TiO_2 composite had an advantage since it could be easily separated from the reaction mixture.

Apart from two widely used semiconducting photocatalysts, some researchers have studied the photocatalytic activity of other semiconductors to find a better photocatalyst that is cheaper, easier to prepared, and able to work under visible light. One potential contender is NiO. In 2011, Yang *et al.*[27] synthesized porous polycrystalline nanowires of NiO using a hydrothermal method. They studied the photocatalytic activity of the prepared catalyst for acid scarlet degradation. The results showed that the synthesized NiO catalyst had a potential to degrade acid scarlet dye at wavelength 365 nm with around 80 percent of degradation in 60 minutes. Even though its photocatalytic activity is better than ordinary NiO nanoparticle, the photocatalytic activity of synthesized porous polycrystalline nanowires of NiO is still less than that of TiO_2.

In 2013, Tie *et al.*[28] systematically investigated various effects of synthesis conditions on the characters and photocatalytic activity under UV light of NiO nanoparticles. They found that different alkali reactant and calcination temperature affected particle size, surface area, band gap, and photocatalytic activity of the synthesized NiO. They also stated that small crystalline NiO (less than 100 nm in size) has better photocatalytic activity because it has shallow trapped holes, which easily reacts with water to generate hydroxyl radical. However, the photocatalytic ability of NiO under UV light reported in this work is not comparable to that of TiO_2 or ZnO. With this information, scientists later discovered several methods to prepare NiO with the enhanced photocatalytic activity. For instance, in 2015, Tianduo *et al.*[29] used a solvothermal method to synthesize ultrathin porous NiO nanosheets, which possess significantly greater photocatalytic activity under UV light than commercial NiO. In the same year, Mahjoub *et al.*[30] synthesized spherical NiO nanoparticles *via* a microemulsion method. The prepared NiO nanoparticles could be used as a photocatalyst for degradation of methyl orange. The results confirmed that the NiO nanoparticles prepared by the microemulsion method has approximately two times better photocatalytic activity than the NiO nanoparticles prepared by a hydrothermal method.

Like TiO_2 and ZnO, there are numbers of literature that used supporting materials to help improving the performance of NiO. For example, In 2015, Yang *et al.*[1] studied the degradation of methylene blue *via* adsorption using graphene oxide and photodegradation using nickel oxide simultaneously. The results showed that graphene oxide adsorbed dye around 70 percent in 80 minutes. Moreover, when the UV light was irradiated, the degradation efficiency increased to 97 percent in 40 minutes. This result clearly demonstrated the synergistic effect between NiO and graphene oxide.

To further improve the photocatalytic ability of semiconductors, scientists have incorporated AuNPs to a composite to use its ability to initiate LSPR. For example, Wu *et al.*[6] deposited AuNPs on the surface of TiO_2 film, then utilized the film as a photocatalyst for MB degradation under simultaneous irradiation of UV and visible light. The results showed that the TiO_2 film incorporated with AuNPs possesses several times greater photocatalytic activity than the TiO_2 film alone. This demonstrated the positive effect of AuNPs on the photocatalytic activity of semiconductors *via* LSPR.

Chapter 2

Experimental section

2.1 Instruments, equipment, and chemicals

2.1.1 Instruments and equipment

1. UV-Vis spectrometer (HP Agilent 8453)
2. Inductively coupled plasma optical emission spectrometer (Perkin Elmer Optima 2100)
3. Transmission electron microscope (JEM-2100, JOEL)
4. X-ray diffractometer (DMAX2200/Ultima+, Rigaku)
4. Analytical balance (Mettler-Toledo)
5. Magnetic stirrer (GEM MS 101)
5. Centrifuge machine (Sanyo Centaur 2)
6. Micropipette (Brand Transferpette®)
7. Quartz cuvette 1.5 mL (Strana Scientific)
8. Safe-lock microcentrifuge tube 1.5 mL (Eppendorf®)

2.1.2 Chemicals

1. Calcium nitrate tetrahydrate ($Ca(NO_3)_2 \cdot 4H_2O$)
2. Ammonium hydrogen phosphate (($NH_4)_2HPO_4$)
3. Iron (II) chloride tetrahydrate ($FeCl_2 \cdot 4H_2O$)
4. Iron (III) chloride hexahydrate ($FeCl_3 \cdot 6H_2O$)
5. Nickel nitrate hexahydrate ($Ni(NO_3)_2 \cdot 6H_2O$)
6. Chloroauric acid ($HAuCl_4$)
7. Poly(ethylene glycol) or PEG
8. Urea
9. Sodium borohydride ($NaBH_4$)
10. Poly(vinylpyrrolidone) or PVP
11. Methylene blue (MB)
12. Methyl orange (MO)
13. 25% NH_3 solution
14. Ethanol, AR grade

All chemicals were used as received without further purification.

2.2 Synthesis of HAp@γ-Fe₂O₃

Maghemite nanoparticle-coated hydroxyapatite (HAp@γ-Fe₂O₃) was prepared by the method described in literature with some adaptations.[31] First, $Ca(NO_3)_2 \cdot 4H_2O$ (3.9359 g) and $(NH_4)_2HPO_4$ (1.3206 g) were separately dissolved in 20 mL of deionized water and each solution was kept in a syringe. Then, $FeCl_2 \cdot 4H_2O$ (0.3728 g), $FeCl_3 \cdot 6H_2O$ (1.0136 g), and 5 mL of deionized water were mixed in a two-necked round-bottom flask. After that, 25% NH_3 solution (15 mL) was injected into the flask through septum. The reaction mixture was stirred under argon atmosphere for 15 minutes. Then, the prepared calcium ion solution was injected in one portion, followed by injecting another portion (15 mL) of NH_3 solution and phosphate solution. The reaction mixture was stirred and heated at 90 ⁰C for 2 hours. Afterward, neodymium magnet was used to separate the material from the reaction mixture. The material was then washed with deionized water. This washing and separating process was repeated until the pH of the mixture was neutral. The obtained slurry material was oven-dried at 60 °C overnight. The obtained dark brown solid powder was characterized by XRD, ICP-OES, and TEM.

2.3 Synthesis of NiO-coated HAp@γ-Fe₂O₃

NiO-coated HAp@γ-Fe₂O₃ (NiO-HAp@γ-Fe₂O₃) was synthesized by the method described in literatures with some adaptations[31]. First, $Ni(NO_3)_2 \cdot 6H_2O$ (5.8444 g), poly(ethylene glycol) (2.0000 g), and urea (4.8000 g) were dissolved in 43 mL of deionized water. Subsequently, HAp@γ-Fe₂O₃ (1.2682 g) was added; and the mixture was stirred at ambient condition for 2 hours. After that, the mixture was poured into a Teflon-lined autoclave reactor and heated at 160 ⁰C for 12 hours. The crude product was separated from the reaction mixture by three sets of washing (with 1:1 ethanol/water mixed solvent) and centrifuging (4000 rpm) process. Next, the crude product was oven-dried at 60 ⁰C overnight and finally calcined at 600 ⁰C for 4 hours. The same procedure was performed with half amount of starting materials except for that of HAp@γ-Fe₂O₃, labeled as 0.5NiO-HAp@γ-Fe₂O₃, was performed with one-fourth amount of starting materials except for that of HAp@γ-Fe₂O₃, labeled as 0.25NiO-HAp@γ-Fe₂O₃, and was performed without HAp@γ-Fe₂O₃, labeled as NiO.

2.4 Impregnation of Au on NiO-HAp@γ-Fe₂O₃

Au-NiO-HAp@γ-Fe₂O₃ was prepared by the method described in literatures with some adaptations[32,33]. Briefly, PVP and HAuCl₄ were mixed with deionized water. The solution was stirred until PVP was completely dissolved. Meanwhile, NaBH₄ was dissolved in deionized water in a separate beaker. Then, NaBH₄ solution was poured into the HAuCl₄ solution in one portion, and the reaction was stirred for 1 hour. Subsequently, NiO-HAp@γ-Fe₂O₃ was added and the reaction mixture was refluxed under argon atmosphere for an hour. The crude product was separated from reaction mixture by three sets of washing (with ethanol/water mixed solvent) and centrifuging (4000 rpm) process. Next, the crude product was oven-dried at 60 °C overnight and finally calcined at 450 °C 4 hours. The same procedure was performed with the same amount of starting materials except for 0.5NiO-HAp@γ-Fe₂O₃, labeled as Au-0.5NiO-HAp@γ-Fe₂O₃, and 0.25NiO-HAp@γ-Fe₂O₃, labeled as Au-0.25NiO-HAp@γ-Fe₂O₃.

2.5 Preparation of organic dye solutions

Stock solutions (300 ppm) of organic dyes, namely methylene blue (MB, Figure 2.1a) and methyl orange (MO, Figure 2.1b) were prepared by diluting each dye (75.0 mg) with deionized water in 250 mL volumetric flasks. Dye solutions used in photocatalytic experiments (7.5 ppm) were prepared by diluting 25 mL of the prepared stock solution in 1000 mL volumetric flask.
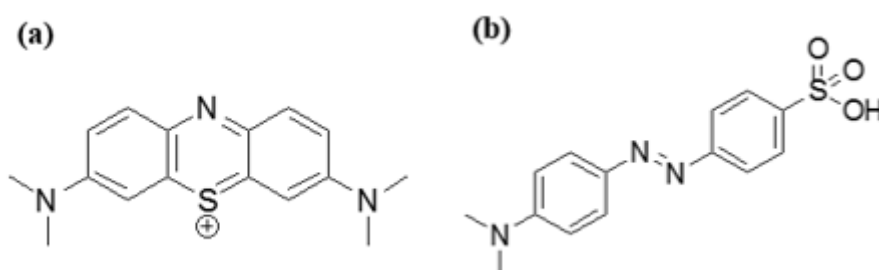
Figure 2.1 Structures of (a) methylene blue, (b) methyl orange.

2.6 Study of photocatalytic performance of synthesized materials

An LED flexible strip (3 meters, 14.4 W) was used as a light source. 20.0 mg of synthesized material was added into a glass bottle filled with 50 mL of 7.5 ppm dye solution. Before illumination, the mixture was stirred in the dark for 60 minutes to

ensure adsorption equilibrium. At a specific time, a certain amount of the suspension (1.5 mL) was taken out and filtrated with a 0.45 μm nylon filter to completely remove the solid material. The photocatalytic performance was monitored by measuring the concentration of remaining organic dyes using UV-Vis spectrophotometer at 664 nm.

2.7 Sample preparation for ICP-OES measurement

The synthesized materials were dissolved in hot concentrated nitric acid. Then, the volume of solution was adjusted to be 25.00 mL. After that, the solution was filtrated with a 0.45 μm nylon filter to eliminate residue. The elemental concentration in the obtained solution was measured by ICP-OES.

Chapter 3

Results and Discussion

3.1 Characterization of prepared materials

3.1.1 X-ray diffractometer (XRD)

The structures of prepared materials were characterized by X-ray diffractometer (DMAX2200/Ultima+, Rigaku). The data was obtained between $2\theta = 20°$ and $80°$. The XRD patterns of HAp@γ-Fe$_2$O$_3$ (Figure 3.1) exhibited peaks corresponding to HAp and γ-Fe$_2$O$_3$ which correlated with the references of HAp (JCPDS PDF 09-0432) and γ-Fe$_2$O$_3$ (JCPDS PDF 05-0637). The diffraction pattern of HAp showed peak at $2\theta \approx$ 25.9°, 31.8°, 32.2°, 32.9°, and 49.5°, corresponding to the (002), (211), (112), (300), and (213) hexagonal planes, respectively, while the diffraction pattern of γ-Fe$_2$O$_3$ illustrated peaks at $2\theta \approx$ 24.1°, 33.0°, 35.6°, 49.5° and 54.2°, corresponding to the (012), (104), (110), (024), and (116) cubic planes, respectively. Therefore, we can confirm that the synthesized HAp@γ-Fe$_2$O$_3$ was successfully prepared. The prepared composite was composed of HAp and γ-Fe$_2$O$_3$ phases.[34]
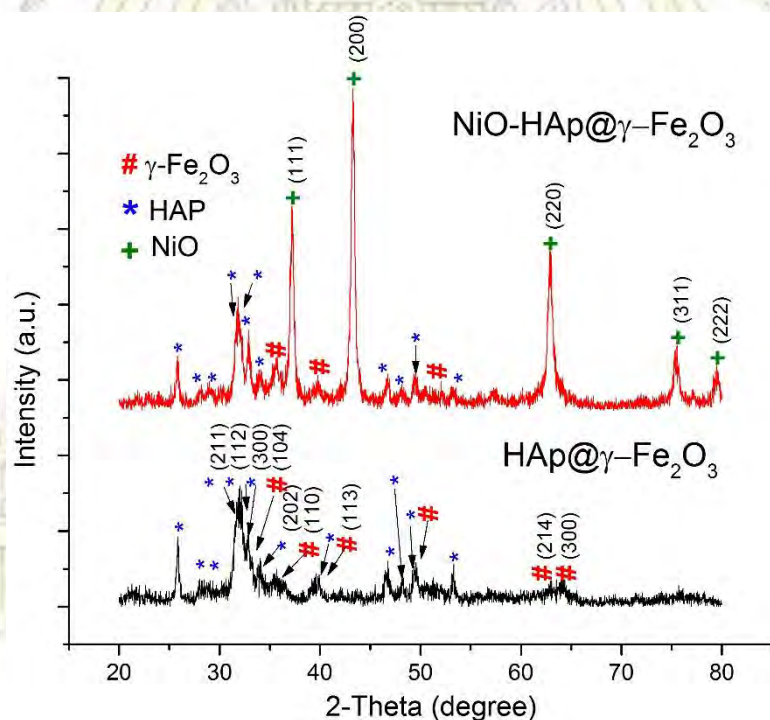

Figure 3.1 XRD patterns of HAp@γ-Fe$_2$O$_3$ and NiO-HAp@γ-Fe$_2$O$_3$.
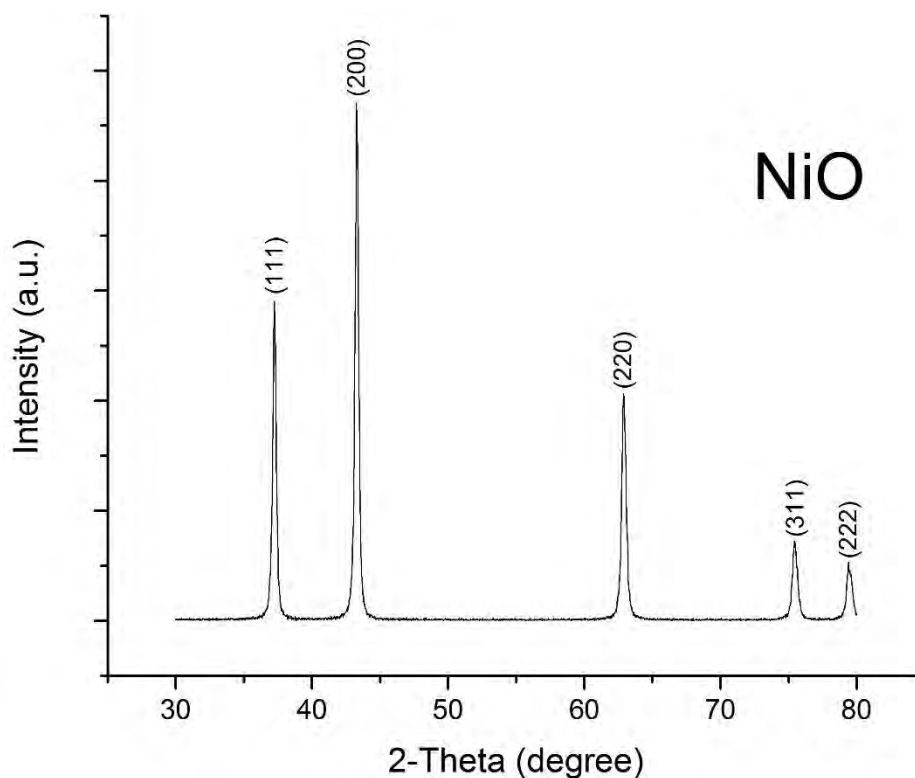
Figure 3.2 XRD pattern of pristine NiO.

The peaks of HAp and iron oxide could also be found in the XRD pattern of NiO-HAp@γ-Fe₂O₃ (Figure 3.1), confirming that HAp and γ-Fe₂O₃ phases were retained. In addition, XRD patterns of the materials also showed peaks of NiO, consistent with the diffraction peaks of cubic NiO reference (JCPDS PDF 89-7130) at $2\theta \approx 37.1°$, $43.1°$, and $62.6°$, correlating with (111), (200), and (220) cubic planes, respectively (Figure 3.2). Therefore, we can confirm that the synthesized NiO-HAp@γ-Fe₂O₃ was composed of NiO phase and doping NiO did not change the crystal structure of HAp@γ-Fe₂O₃. Moreover, comparing the XRD pattern of NiO-HAp@γ-Fe₂O₃ with that of pristine NiO, the XRD pattern of NiO in the composite was broader, indicating smaller crystalline size of NiO in the composite. This information has an agreement with the calculated crystalline size of NiO based on Scherrer equation (Table 3.1), while the crystalline sizes of HAp and γ-Fe₂O₃ remain unchanged.

Table. 3.1 The crystal sizes of synthesized materials calculated by Scherrer equation

Material	NiO crystal size (nm)	HAp crystal size (nm)	γ-Fe$_2$O$_3$ crystal size (nm)
NiO	37.2	-	-
HAp@γ-Fe$_2$O$_3$	-	35.5	8.4
NiO-HAp@γ-Fe$_2$O$_3$	21.4	35.5	8.4
Au-NiO-HAp@γ-Fe$_2$O$_3$	21.4	35.5	8.4
Au-0.5NiO-HAp@γ-Fe$_2$O$_3$	19.0	35.5	8.4
Au-0.25NiO-HAp@γ-Fe$_2$O$_3$	9.5	35.5	8.4

The XRD patterns of Au-NiO-HAp@γ-Fe$_2$O$_3$ (Figure 3.3) were consistent with references of HAp (JCPDS PDF 09-0432), γ-Fe$_2$O$_3$ (JCPDS PDF 05-0637) and NiO (JCPDS PDF 89-7130). Therefore, the results confirmed phase existence of HAp, γ-Fe$_2$O$_3$, and NiO in the composite.
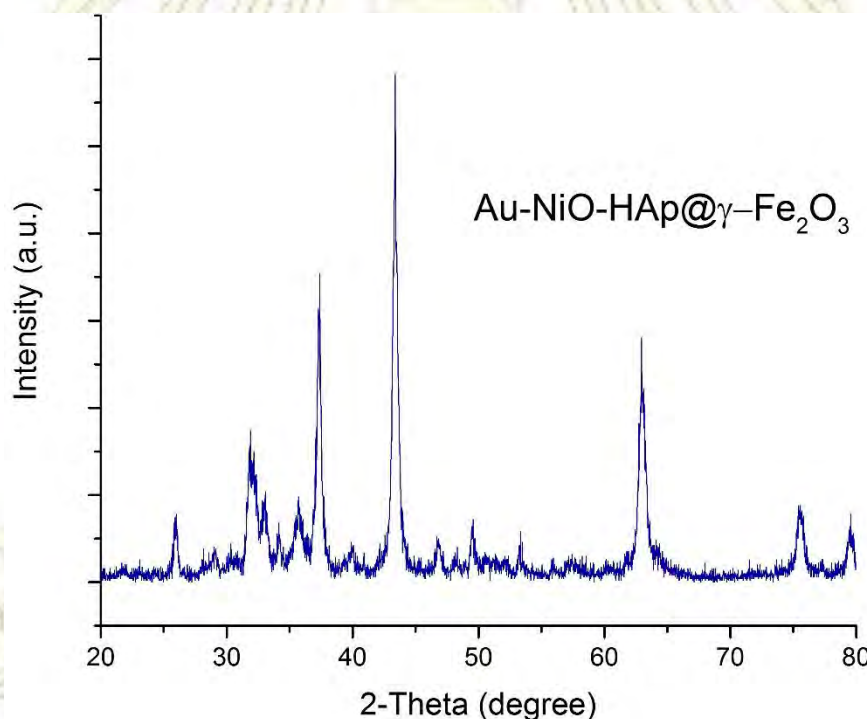
Figure 3.3 XRD pattern of Au-NiO-HAp@γ-Fe$_2$O$_3$.

The peak intensity of NiO was correlated with the amount of NiO in the composite as shown in Figure 3.4. The NiO crystallinity and crystalline size of nickel oxide-gold composites also increased as the amount of initial Ni source increased.

However, peaks of Au particle were not observed in the XRD patterns of the synthesized material probably due to a tiny amount of Au present in the composites.
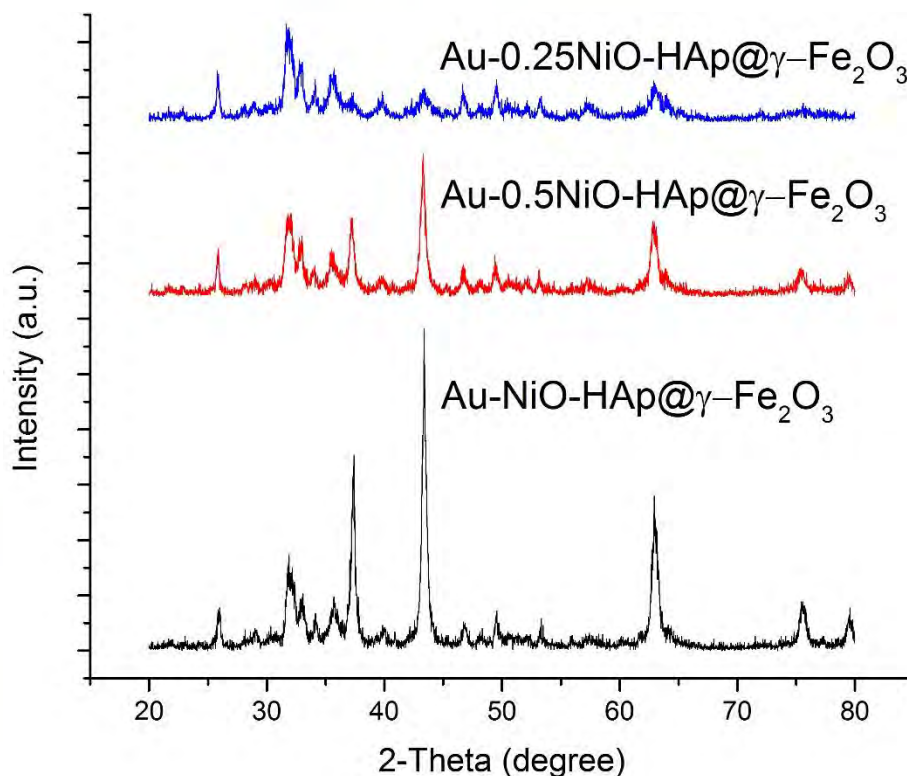
Figure 3.4 XRD patterns of Au-NiO-HAp@γ-Fe$_2$O$_3$ with different amount of NiO.

3.1.2 Transmission electron microscope (TEM)

The morphology of prepared materials was characterized by TEM. Figure 3.5a shows the TEM image of HAp@γ-Fe$_2$O$_3$, illustrating the black clumps of γ-Fe$_2$O$_3$ nanoparticles surrounded by needle-like crystals of HAp. This morphology is desirable since the surrounded HAp prevents γ-Fe$_2$O$_3$ aggregation, and provides nucleation sites for further metal ions impregnation. The average particle size of HAp is 53.5±16.2 nm in length and 9.0±1.9 nm in width, and the average particle size of γ-Fe$_2$O$_3$ is 6.7±2.6 nm.

The TEM image of NiO-HAp@γ-Fe$_2$O$_3$ is shown in Figure 3.5b. As can be seen, the black clumps of γ-Fe$_2$O$_3$ and the grey needle-like crystals of HAp remain intact, but both components look thicker because γ-Fe$_2$O$_3$ and HAp are covered by NiO particles. The average particle size of NiO-HAp is 55.8±16.5 nm in length and 27.1±6.2 nm in

width, and the average particle size of γ-Fe$_2$O$_3$ is 15.5±6.4 nm. The results are consistent with the calculated crystalline size based on Scherrer's equation from XRD results.
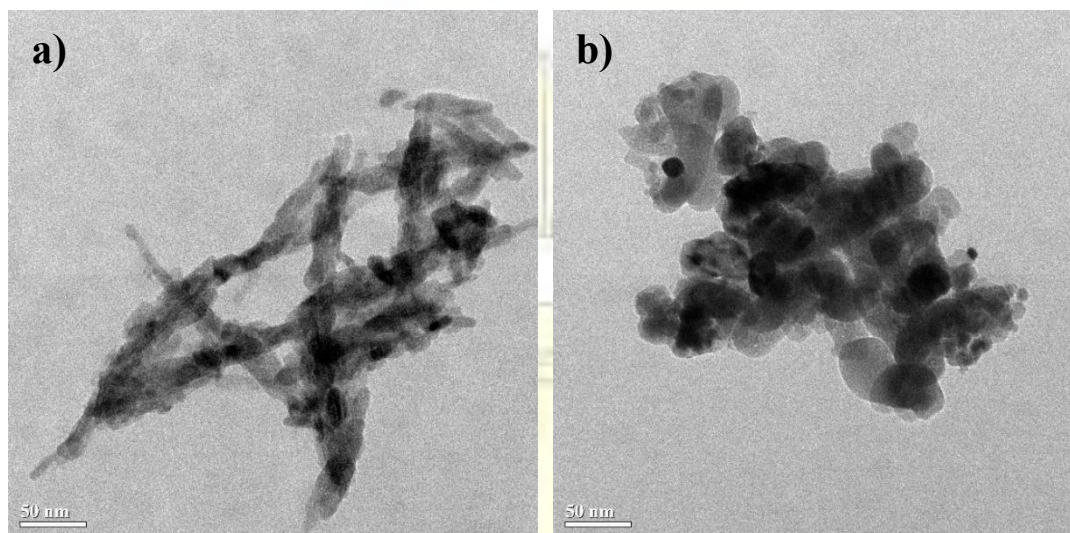
Figure 3.5 TEM images of a) HAp@γ-Fe$_2$O$_3$ b) NiO-HAp@γ-Fe$_2$O$_3$.

In order to avoid the complication caused by multi-component, the Au-Hap was synthesized using the same procedure as Au impregnation on NiO-HAp@γ-Fe$_2$O$_3$, except that HAp was used instead of NiO-HAp@γ-Fe$_2$O$_3$.The TEM image of Au-HAp (Figure 3.6) shows the uniform distribution of spherical Au nanoparticles on the surface of HAp. The average particle size of gold nanoparticle is 3.3 ± 0.9 nm and the size distribution of the nanoparticles is shown in the inset in Figure 3.6.

Figure 3.6 TEM image of Au-HAp (inset: size distribution of gold nanoparticles).

3.1.3 Inductively coupled plasma optical emission spectrophotometer (ICP-OES)

Since the synthesized materials are composed of several compositions, qualitative characterization of each component using only TEM was not enough. Moreover, XRD pattern of Au-NiO-HAp@γ-Fe$_2$O$_3$ did not exhibit any characteristic pattern of Au due to its small size. Therefore, ICP-OES was used to confirm the existence of metals (e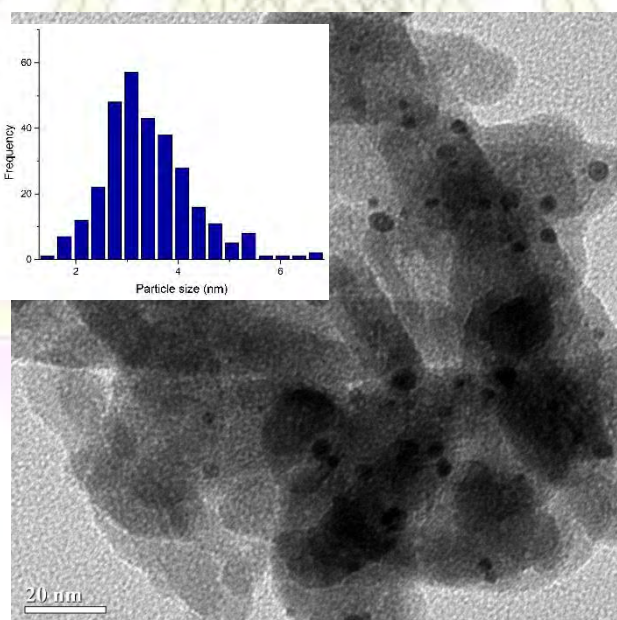specially Au) and determine their amount in the prepared composites. Table 3.1 lists the metal amount in each synthesized material. As can be seen, the amount of nickel in the nickel oxide-gold composites was decreased when the initial amount of Ni source used in the preparation was decreased (6.5, 4.7, and 2.0 mmol/g in Au-NiO-HAp@γ-Fe$_2$O$_3$, Au-0.5NiO-HAp@γ-Fe$_2$O$_3$, and Au-0.25NiO-HAp@γ-Fe$_2$O$_3$, respectively). In addition, ICP-OES results confirmed that small amount of Au was successfully incorporated in the Au-NiO-HAp@γ-Fe$_2$O$_3$ composite. However, the Ni/Au ratio did not follow the trend since the amount of Au in Au-0.5NiO-HAp@γ-Fe$_2$O$_3$ is significantly lower than that in the other materials.

Table. 3.2 Nickel and gold composition in prepared composites and their ratio.

Composites	Ni (mmol/g)	Au (μmol/g)	Ni/Au ratio
Au-HAp@γ-Fe$_2$O$_3$	-	2.5	-
NiO-HAp@γ-Fe$_2$O$_3$	6.5	-	-
Au-NiO-HAp@γ-Fe$_2$O$_3$	6.5	3.6	2560
Au-0.5NiO-HAp@γ-Fe$_2$O$_3$	4.7	1.4	3357
Au-0.25NiO-HAp@γ-Fe$_2$O$_3$	2.0	3.9	513

3.2 Photocatalytic activity of prepared materials

To evaluate the photocatalytic activity of prepared materials, we selected cationic methylene blue (MB) as a model dye.[1,35] Previous researches showed that MB is quite stable under visible light.[36,37] Chang and his collaborators[33] showed that methylene blue negligibly degraded after 80 minutes of visible light irradiation (Figure 3.7). According to this knowledge, after we had finished synthesizing Au-NiO-HAp@γ-Fe$_2$O$_3$, we decided to carry on the photocatalytic degradation of MB under visible light using the prepared materials, including AuNiO-HAp@γ-Fe$_2$O$_3$, Au0.5NiO-

HAp@γ-Fe$_2$O$_3$, Au0.25NiO-HAp@γ-Fe$_2$O$_3$, NiO-HAp@γ-Fe$_2$O$_3$, Au-HAp@γ-Fe$_2$O$_3$, HAp@γ-Fe$_2$O$_3$, NiO-HAp, NiO, and HAp. The results are shown in Figure 3.8.
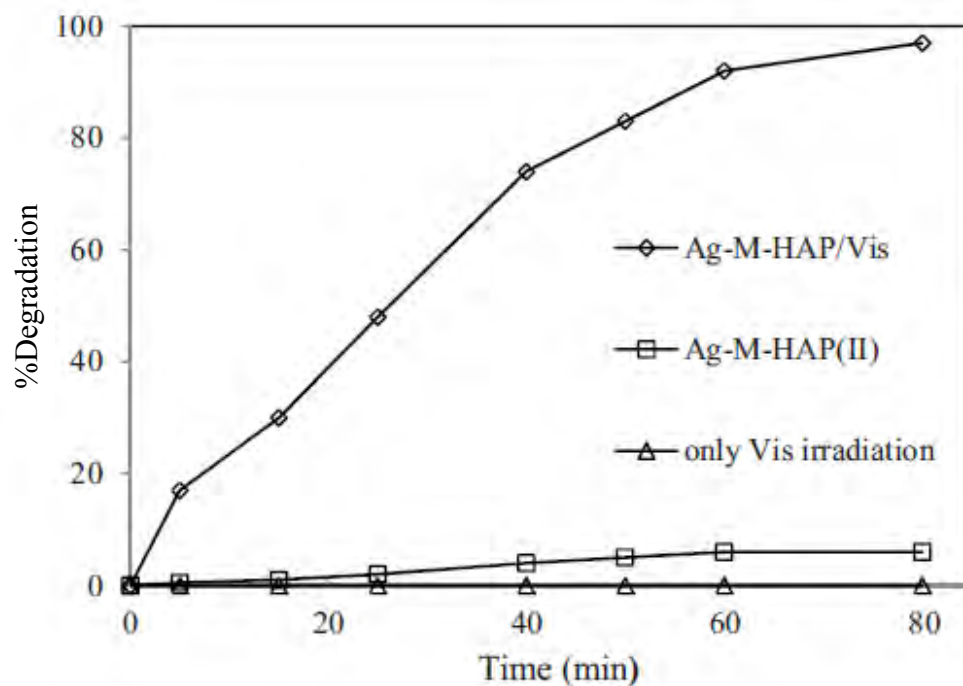

Figure 3.7 Photodegradation of MB under visible light with and without catalyst.[36]
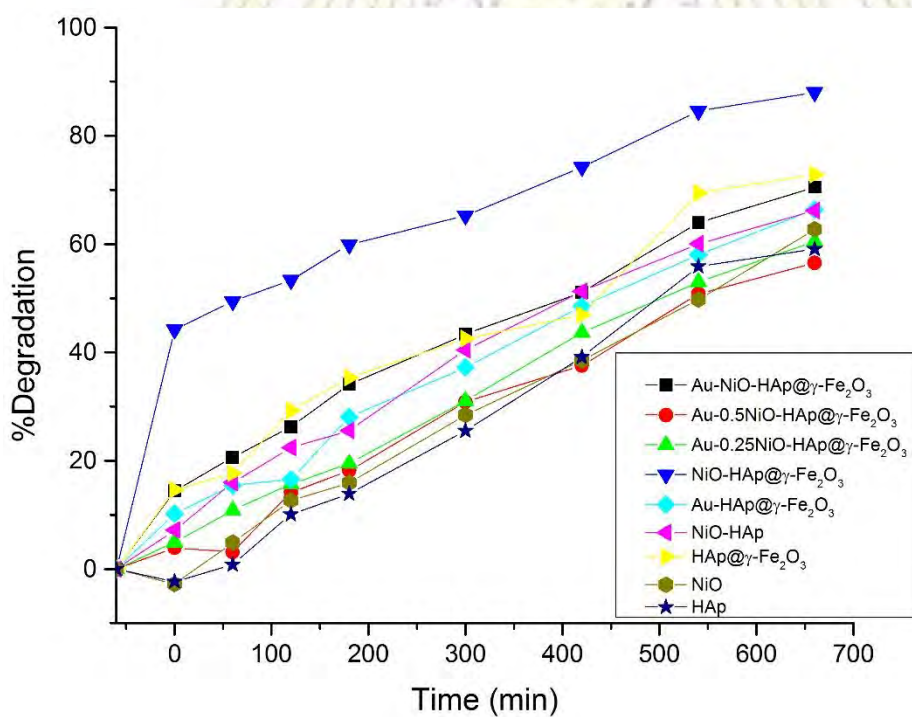

Figure 3.8 Photocatalytic degradation of MB over various materials.

As can be seen, all prepared materials exhibited photocatalytic activity toward MB degradation under visible light with similar degree of degradation. As shown in Table 3.3, after 660 minutes of visible light irradiation, the %MB degradation of all materials except NiO-HAp@γ-Fe$_2$O$_3$ was in the range of 56-73%, while NiO-HAp@γ-Fe$_2$O$_3$ showed the highest %degradation of 88%. Since the degradation process comprises of adsorption in the dark and photodegradation under visible light. The effect of photodegradation was clarified by subtracting %MB degradation caused by adsorption prior to irradiation from the total %MB degradation (Table 3.3 and Figure 3.9). The results were even more surprising since the corrected %degradation was roughly equal for all materials.

Table 3.3 % MB degradation caused by photodegradation and adsorption

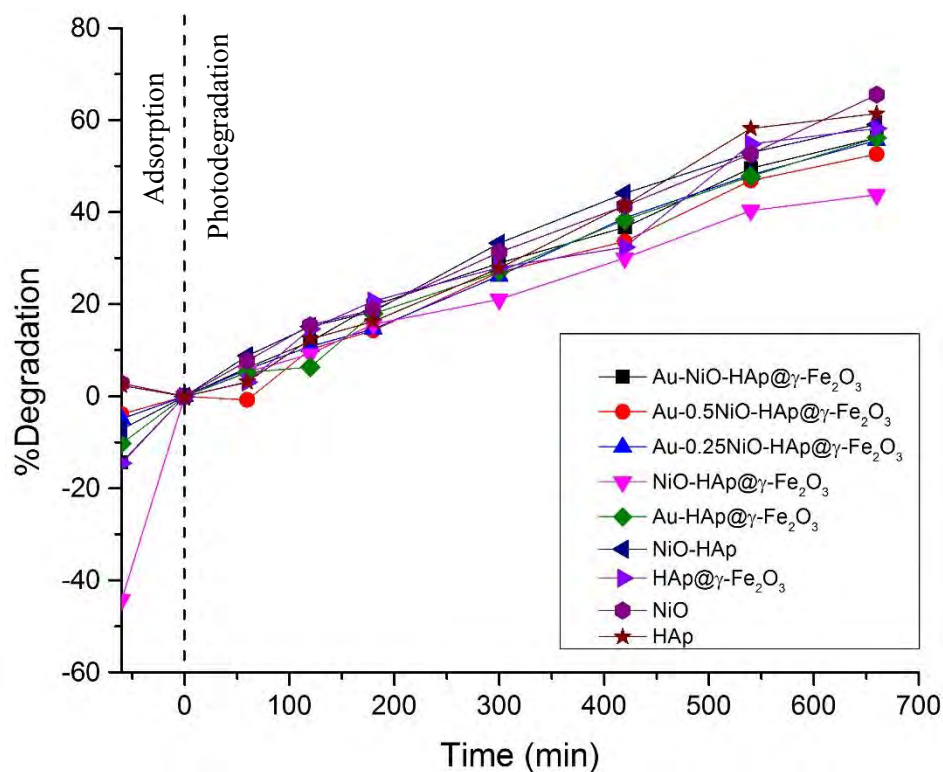| Material	%MB degradation after 660 min irradiation	%MB degradation after 60 min adsorption in the dark	Corrected %MB degradation after 660 min irradiation
Au-NiO-HAp@Fe$_2$O$_3$	70.51	14.39	56.12
Au-0.5NiO-HAp@Fe$_2$O$_3$	56.52	3.93	52.59
Au-0.25NiO-HAp@Fe$_2$O$_3$	60.52	4.94	55.58
NiO-HAp@Fe$_2$O$_3$	87.98	44.22	43.76
Au-HAp@Fe$_2$O$_3$	66.37	10.24	56.13
NiO-HAp	66.18	7.18	59.00
HAp@Fe$_2$O$_3$	72.81	14.61	58.20
NiO	62.70	0.00	62.70
HAp	59.08	0.00	59.08

Figure 3.9 Corrected results (setting the %MB degradation to zero when the irradiation starts) of photocatalytic degradation of MB over various materials.

There are two possible explanations regarding these unexpected results. First, all materials used in the experiment (even the supporting material like HAp) showed the photocatalytic ability for MB degradation. Second, there were some unanticipated effects occurring in every experiment, causing the similar efficiency for MB degradation.

At first, we expected that the heat generated from LED light might have some effects to the photodegradation of MB. To clarify this, the experiment was performed without both the addition of a catalyst and the irradiation from LED light source. Instead, the reaction was carried out at 60 °C in a water bath. As shown in Figure 3.10, there is only slight degradation of MB after the adsorption period. Therefore, we can conclude that heat has very little effect on the photocatalytic degradation of MB so it could not explain the similar photodegradation degree of MB in the presence of different materials.
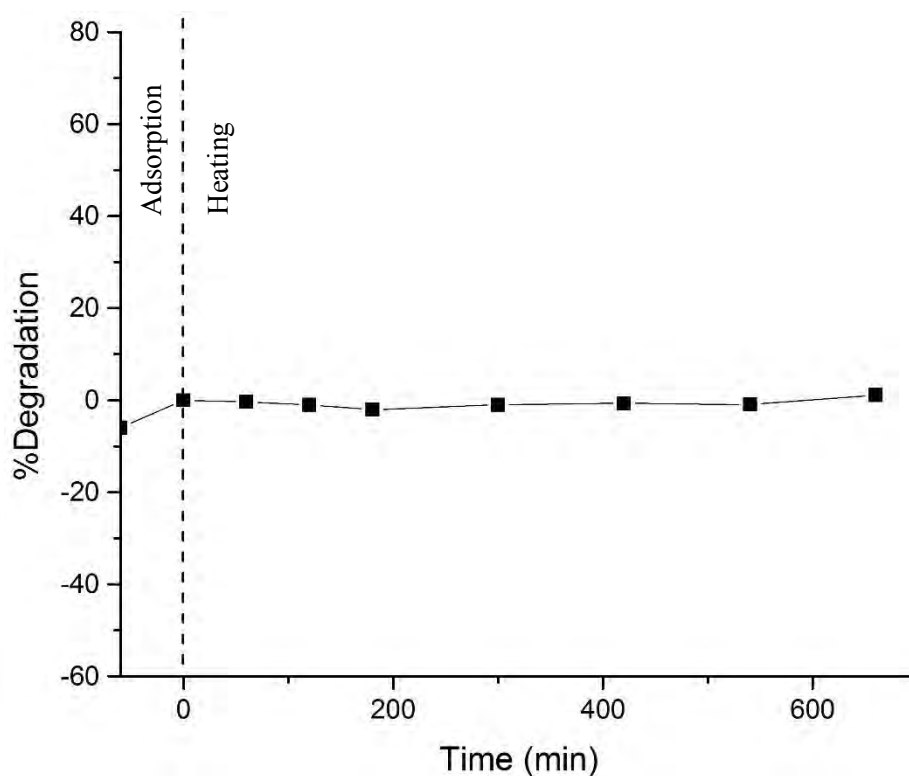
Figure 3.10 Corrected results of degradation of MB caused by heat (60 °C) only.

To eliminate factors originating from MB, we instead used methyl orange (MO), anionic dye, which is another dye widely accepted as a model to evaluate the photocatalytic activity of catalysts.[38,39] The results are illustrated in Figure 3.11, which clearly shows that there is very little degradation in all cases during the irradiation period (0-700 min). These results were confusing since it confirms that the degradation found in case of MB does not come from the materials. The only possible explanation is MB can degrade by itself under visible light irradiation.
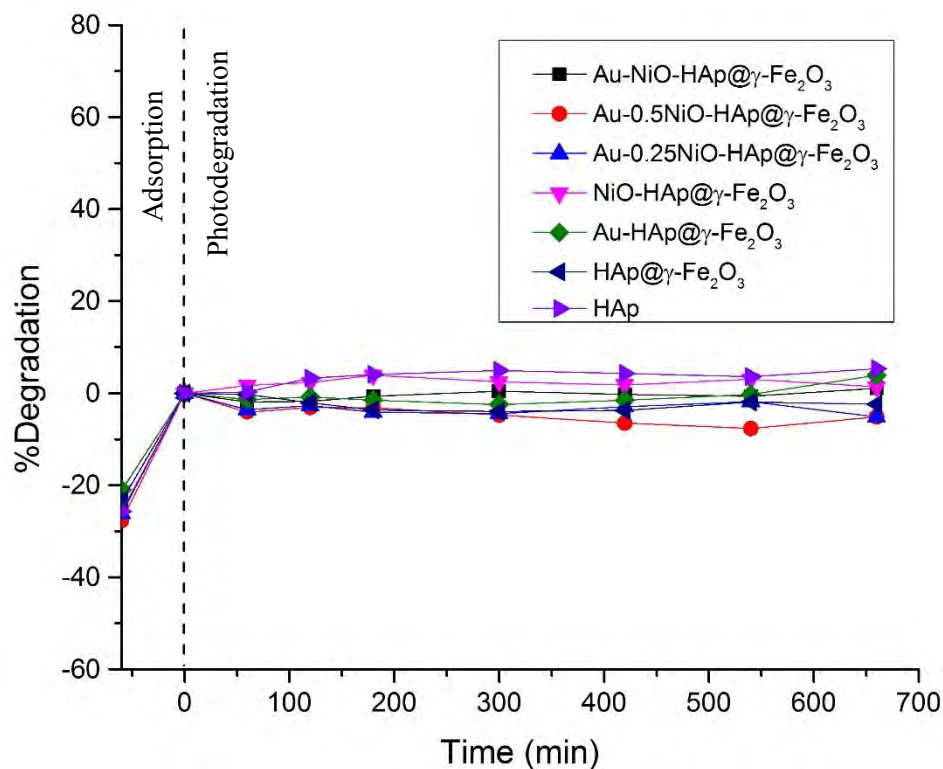
Figure 3.11 Corrected results of photocatalytic degradation of MO over various materials.

To prove the idea that MB can degrade by itself under visible light irradiation, the same experiment was done without adding any material into MB solution. The result is shown in Figure 3.12. The result clearly showed that MB can degrade itself through the photolysis process (i.e. catalyst is not needed), and unfortunately proved that our prepared materials do not have significant photocatalytic activity. To explain why there is apparently no literature discussing on the photolysis of MB, we should take a closer look at the photodegradation results from literature (Figure 3.7) which shows a negligible degradation over a relatively short period of time (0-80 minutes) which misled us to believe that MB could not degrade by itself. To the best of our knowledge, there was no literature evaluating photocatalytic activity by operating the reaction more than three hours, so we could not see the long term self-photolysis factor earlier.

Figure 3.12 Photolysis of MB under visible light.

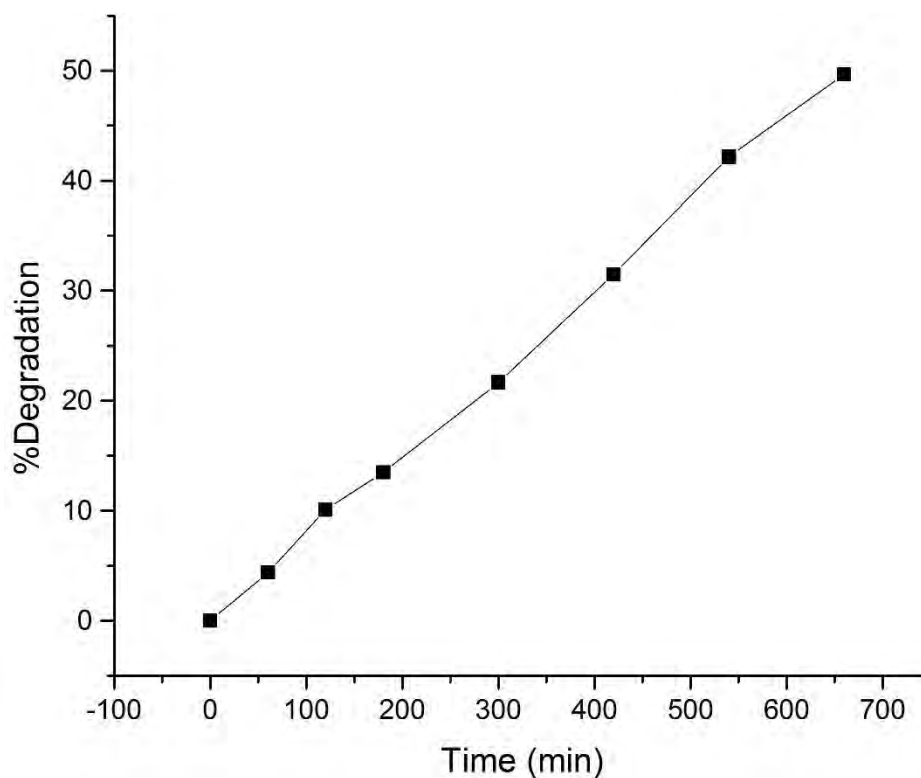One possible reason why the prepared materials did not have photocatalytic property as we expected is the poor overlap between the frontier bands of HAp and NiO. Although HAp and NiO have similar band gaps (3.6 eV for HAp and 3.6-4.0 eV for NiO)[40], the absolute energy of their valence band and conduction band might not be close in energy and the effective overlap between them is not possible. As a consequence, since the band gap of NiO is equal to the energy of light at 310-345 nm wavelength, without the overlapping from HAp, NiO cannot absorb energy from the visible light (>400 nm). Another plausible explanation is, since TEM image shows that NiO particles completely cover the surface of HAp@γ-Fe$_2$O$_3$, band gap of NiO in this case may not equal to that of typical NiO nanoparticles reported in the aforementioned literature. Instead, the band gap of NiO in the prepared materials may be much larger because the particle size may be smaller. Moreover, even though our materials can absorb visible light, we could not rule out the effect caused by the fast recombination of electron-hole pairs, which significantly suppresses the photocatalytic activity of semiconducting materials.[41]

Chapter 4

Conclusions

We successfully synthesized novel nickel oxide-gold supported on magnetic nanoparticle-hydroxyapatite composites via co-precipitation and impregnation methods. The characterization exhibited that the as-prepared material contains γ-Fe_2O_3, HAp, and NiO using XRD, and gold using ICP-OES and TEM. In addition, XRD results indicated that the composites contain different crystalline sizes of NiO, and the amount of NiO depends on the added initial nickel source, which is consistent with the ICP-OES and TEM results. The morphology from TEM shows distribution of gold nanoparticles with the size around 3.3 nm, and increment of HAp and γ-Fe_2O_3 size because of NiO coated on their surface. The results from photocatalytic activity study showed that there is no significant dye degradation neither under UV nor visible light using the prepared materials as photocatalysts. The type of organic dye and heat also did not cause the degradation of organic dye to occur. The observed-degradation of methylene blue came from photolysis of methylene blue itself.

Further improvement is possible, such as changing the supporting material or preparation of nickel oxide to change absolute energy level and energy gap, or lowering the wavelength of irradiation light. Other possible applications of these novel materials are adsorbents, catalysts for biomass conversion, dye sensitized solar cells or biosensors.

Bibliography

(1)   Rong, X.; Qiu, F.; Zhang, C.; Fu, L.; Wang, Y.; Yang, D. Adsorption–Photodegradation Synergetic Removal of Methylene Blue from Aqueous Solution by NiO/Graphene Oxide Nanocomposite. *Powder Technol.* **2015**, *275*, 322–328.

(2)   Atalay, S.; Ersöz, G. *Novel Catalysts in Advanced Oxidation of Organic Pollutants*; 2016.

(3)   Manigandan, R.; Giribabu, K.; Suresh, R.; Munusamy, S.; Praveen Kumar, S.; Muthamizh, S.; Stephen, A.; Narayanan, V. Characterization and Photocatalytic Activity of Nickel Oxide Nanoparticles. *Int. J. ChemTech Res.* **2014**, *6* (6 SPEC. ISS.), 3395–3398.

(4)   Mahlambi, M. M.; Mishra, A. K.; Mishra, S. B.; Krause, R. W.; Mamba, B. B.; Raichur, A. M. E Ff Ect of Metal Ions (Ag , Co , Ni , and Pd) on the Visible Light Degradation of Rhodamine B by Carbon-Covered Alumina- Supported TiO$_2$ in Aqueous Solutions. *J. Nanotechnol.* **2015**, *2015*.

(5)   Li, A.; Zhang, P.; Chang, X.; Cai, W.; Wang, T.; Gong, J. Gold Nanorod@TiO$_2$ Yolk-Shell Nanostructures for Visible-Light-Driven Photocatalytic Oxidation of Benzyl Alcohol. *Small* **2015**, 1892–1899.

(6)   Chen, J.; Wu, C. S.; Wu, P. C.; Tsai, D. P. Improved Photocatalytic Activity of Shell-Isolated Plasmonic Photocatalyst Au @ SiO$_2$ / TiO$_2$ by Promoted LSPR. *J. Phys. Chem. C,* **2012**. *166*(50), 26535-26542.

(7)   Hara, T.; Kaneta, T.; Mori, K.; Mitsudome, T.; Mizugaki, T.; Ebitani, K.; Kaneda, K. Magnetically Recoverable Heterogeneous Catalyst: Palladium Nanocluster Supported on Hydroxyapatite-Encapsulated γ-Fe$_2$O$_3$ Nanocrystallites for Highly Efficient Dehalogenation with Molecular Hydrogen. *Green Chem.* **2007**, *9* (11), 1246–1251.

(8)   Linh, N. T. T.; Tuan, P. D.; Dzung, N. V. The Shifts of Band Gap and Binding Energies of Titania/hydroxyapatite Material. *J. Compos.* **2014**, *2014*, 283034.

(9)   Ghicov, A.; Schmuki, P. Self-Ordering Electrochemistry: A Review on Growth and Functionality of TiO$_2$ Nanotubes and Other Self-Aligned MO(x) Structures. *Chem. Commun. (Camb).* **2009**, No. 20, 2791–2808.

(10)   Shylesh, S.; Schünemann, V.; Thiel, W. R. Magnetically Separable

Nanocatalysts: Bridges between Homogeneous and Heterogeneous Catalysis. *Angew. Chemie - Int. Ed.* **2010**, *49* (20), 3428–3459.

(11) Yu, P. Y.; Cardona, M. *Fundamentals of Semiconductors: Physics and Materials Properties*; 2005; Vol. 1.

(12) Yuzawa, H.; Yoshida, T.; Yoshida, H. Gold Nanoparticles on Titanium Oxide Effective for Photocatalytic Hydrogen Formation under Visible Light. *Appl. Catal. B Environ.* **2012**, *115–116*, 294–302.

(13) Ma, L.; Jia, I.; Guo, X.; Xiang, L. Current Status and Perspective of Rare Earth Catalytic Materials and Catalysis. *Chinese J. Catal.* **2014**, *35* (2), 108–119.

(14) Gold Nanoparticle Properties http://www.cytodiagnostics.com/store/pc/Gold-Nanoparticle-Properties-d2.htm (accessed Feb 15, 2017).

(15) Link, S.; El-Sayed, M. a. Size and Temperature Dependence of the Plasmon Absorption of Colloidal Gold Nanoparticles. *J. Phys. Chem. B* **1999**, *103* (21), 4212.

(16) Derkachova, A.; Kolwas, K.; Demchenko, I. Dielectric Function for Gold in Plasmonics Applications: Size Dependence of Plasmon Resonance Frequencies and Damping Rates for Nanospheres. *Plasmonics* **2016**, *11* (3), 941–951.

(17) Thermo Spectronic. Basic UV-Vis Theory , Concepts and Applications Basic. *ThermoSpectronic* **2013**, 1–28.

(18) Block Diagram UV Vis Spectrophotometer http://darsi.org/block-diagram-uv-vis-spectrophotometer (accessed Feb 15, 2017).

(19) Hill, S. J. *Inductively Coupled Plasma Spectrometry and Its Applications*; 2007.

(20) Test of an Echelle Spectrograph http://www.astrosurf.com/buil/echelle/first.htm (accessed Feb 15, 2017).

(21) Bunaciu, A. A.; Udristioiu, E. G.; Aboul-Enein, H. Y. X-Ray Diffraction: Instrumentation and Applications. *Crit. Rev. Anal. Chem.* **2015**, *45* (4), 289–299.

(22) No TitleIntroduction to Introduction to Transmission/Scanning Transmission Transmission/Scanning Transmission Electron Microscopy and Microanalysis http://tpm.amc.anl.gov/Lectures/Zaluzec-1-Instrumentation.ppt.pdf (accessed Jan 28, 2017).

(23) Egerton, R. F. *Physical Principles of Electron Microscopy*; 2005; Vol. 24.

(24) Khattab, I. a.; Ghaly, M. Y.; Österlund, L.; Ali, M. E. M.; Farah, J. Y.; Zaher,

F. M.; Badawy, M. I. Photocatalytic Degradation of Azo Dye Reactive Red 15 over Synthesized Titanium and Zinc Oxides Photocatalysts: A Comparative Study. *Desalin. Water Treat.* **2012**, *48* (1–3), 120–129.

(25) Ameen, S.; Shaheer Akhtar, M.; Seo, H. K.; Shin, H. S. Mineralization of Rhodamine 6G Dye over Rose Flower-like ZnO Nanomaterials. *Mater. Lett.* **2013**, *113*, 20–24.

(26) Xie, J.; Meng, X.; Zhou, Z.; Li, P.; Yao, L.; Bian, L.; Gao, X.; Wei, Y. Preparation of Titania/hydroxyapatite (TiO$_2$/HAp) Composite Photocatalyst with Mosaic Structure for Degradation of Pentachlorophenol. *Mater. Lett.* **2013**, *110*, 57–60.

(27) Zhang, L.; An, L.; Liu, B.; Yang, H. Synthesis and Photocatalytic Activity of Porous Polycrystalline NiO Nanowires. *Appl. Phys. A Mater. Sci. Process.* **2011**, *104* (1), 69–75.

(28) Wan, X.; Yuan, M.; Tie, S. L.; Lan, S. Effects of Catalyst Characters on the Photocatalytic Activity and Process of NiO Nanoparticles in the Degradation of Methylene Blue. *Appl. Surf. Sci.* **2013**, *277* (3), 40–46.

(29) Qing, Z.; Haixia, L.; Huali, L.; Yu, L.; Huayong, Z.; Tianduo, L. Solvothermal Synthesis and Photocatalytic Properties of NiO Ultrathin Nanosheets with Porous Structure. *Appl. Surf. Sci.* **2015**, *328*, 525–530.

(30) Fazlali, F.; Mahjoub, A. R.; Abazari, R. A New Route for Synthesis of Spherical NiO Nanoparticles via Emulsion Nano-Reactors with Enhanced Photocatalytic Activity. *Solid State Sci.* **2015**, *48*, 263–269.

(31) Sajjadifar, S.; Abbasi, Z.; Rezaee Nezhad, E.; Moghaddam, M. R.; Karimian, S.; Miri, S. Ni^{2+} Supported on Hydroxyapatite-Core-Shell γ-Fe$_2$O$_3$ Nanoparticles: A Novel, Highly Efficient and Reusable Lewis Acid Catalyst for the Regioselective Azidolysis of Epoxides in Water. *J. Iran. Chem. Soc.* **2014**, *11* (2), 335–340.

(32) Song, X.; Gao, L. Facile Synthesis and Hierarchical Assembly of Hollow Nickel Oxide Architectures Bearing Enhanced Photocatalytic Properties. **2008**, 15299–15305.

(33) Dang, X.; Zhang, X.; Lu, Z.; Yang, Z.; Dong, X.; Zhang, X.; Ma, C.; Ma, H.; Xue, M.; Shi, F. Construction of Au@TiO$_2$/graphene Nanocomposites with Plasmonic Effect and Super Adsorption Ability for Enhanced Visible-Light-Driven Photocatalytic Organic Pollutant Degradation. *J. Nanoparticle Res.*

2014, *16* (2), 2–9.

(34)   Zhang, Z.; Yuan, Z.; Tang, D.; Ren, Y.; Lv, K.; Liu, B. Iron Oxide Encapsulated by Ruthenium Hydroxyapatite as Heterogeneous Catalyst for the Synthesis of 2,5-Diformylfuran. *ChemSusChem* **2014**, *7* (12), 3496–3504.

(35)   Zhang, J.; Wang, P.; Sun, J.; Jin, Y. High-Efficiency Plasmon-Enhanced and Graphene-Supported Semiconductor/metal Core-Satellite Hetero-Nanocrystal Photocatalysts for Visible-Light Dye Photodegradation and H2 Production from Water. *ACS Appl. Mater. Interfaces* **2014**, *6* (22), 19905–19913.

(36)   Valizadeh, S.; Rasoulifard, M. H.; Dorraji, M. S. S. Modified Fe3O4-Hydroxyapatite Nanocomposites as Heterogeneous Catalysts in Three UV, Vis and Fenton like Degradation Systems. *Appl. Surf. Sci.* **2014**, *319*, 358–366.

(37)   Chang, Q.; Li, K. K.; Hu, S. L.; Dong, Y. G.; Yang, J. L. Hydroxyapatite Supported N-Doped Carbon Quantum Dots for Visible-Light Photocatalysis. *Mater. Lett.* **2016**, *175*, 44–47.

(38)   Kaur, J.; Bansal, S.; Singhal, S. Photocatalytic Degradation of Methyl Orange Using ZnO Nanopowders Synthesized via Thermal Decomposition of Oxalate Precursor Method. *Phys. B Condens. Matter* **2013**, *416*, 33–38.

(39)   Al-Qaradawi, S.; Salman, S. R. Photocatalytic Degradation of Methyl Orange as a Model Compound. *J. Photochem. Photobiol. A Chem.* **2002**, *148* (1–3), 161–168.

(40)   Motevalli, K.; Zarghami, Z.; Panahi-Kalamuei, M. Simple, Novel and Low-Temperature Synthesis of Rod-like NiO Nanostructure via Thermal Decomposition Route Using a New Starting Reagent and Its Photocatalytic Activity Assessment. *J. Mater. Sci. Mater. Electron.* **2016**, *27* (5), 4794–4799.

(41)   Pan, D.; Jiao, J.; Li, Z.; Guo, Y.; Feng, C.; Liu, Y.; Wang, L.; Wu, M. Efficient Separation of Electron-Hole Pairs in Graphene Quantum Dots by TiO2 Heterojunctions for Dye Degradation. *ACS Sustain. Chem. Eng.* **2015**, *3* (10), 2405–2413.

Biography

Name: Apakorn Phasuk

Date and Place of birth: October 20th, 1994. Bangkok, Thailand.

Elementary School:

2001-2006 Kositsamosorn Elementary School, Bangkok.

Secondary School:

2007-2012 Satri Wat Rakhang School, Bangkok.

University Education:

2013-2016 B.Sc. (Honors program) in Chemistry, Department of

Chemistry, Faculty of Science, Chulalongkorn University, Bangkok.

Address: 2 Room 50 Soi Itsaraphap 44, Itsaraphap rd., Ban Chang Lo,

Bangkok Noi, Bangkok, 10700.